

UNIVERSITÄT STUTTGART

MASTERARBEIT

Design of a Zeeman slower for a
second generation experimental
setup on quantum degenerate
Dysprosium gases

Julian Kluge

supervisors

Prof. Dr. Tilman PFAU
Prof. Dr. Peter MICHLER

June 4, 2019

Statutory declaration

I herewith declare that I have composed the present thesis myself and without use of any other than the cited sources and aids. Sentences or parts of sentences quoted literally are marked as such; other references with regard to the statement and scope are indicated by full details of the publications concerned. The thesis in the same or similar form has not been submitted to any examination body and has not been published. This thesis was not yet, even in part, used in another examination or as a course performance.

Place/Date:

Signature:

Zusammenfassung

Innerhalb der letzten Jahre haben Systeme aus ultrakalten dipolaren Atomen eine große Aufmerksamkeit erfahren. Ultrakalte Quantengassysteme können verwendet werden, um Festkörperstrukturen zu modellieren oder Eigenschaften von Bose-Hubbard Systemen zu untersuchen. In einem Quantengasmikroskop werden die Atome in ein optisches Gitter geladen. Die Wahl eines geringen Gitterabstands erlaubt die genauere Untersuchung der dipolaren Wechselwirkung zwischen den einzelnen Dysprosiumatomen, welche ein hohes magnetisches Moment aufweisen. Spezielle Abbildungstechniken erlauben eine hohe Auflösung, sogar unterhalb des Abbe-Limits.

Im Rahmen dieser Arbeit wurde ein neuer experimenteller Aufbau zur Erzeugung ultrakalter Dysprosiumatome entworfen. Dabei wurde sich vor allem auf die Planung des dafür benötigten Vakuumabschnitts fokussiert. Zur Erzeugung des Atomstrahls wird Dysprosium auf Temperaturen über 1250 °C erhitzt. Um die schnellen Atome abbremsen und in einer magneto-optischen Falle einfangen zu können, wurde ein Zeemanabbremsler für Dysprosium entwickelt und gebaut. Der Zeemanabbremsler in Spin-flip Konfiguration erlaubt ein Abbremsen der Atome auf eine Endgeschwindigkeit von 8 m/s.

Eine weitere untersuchte Anforderung des neuen experimentellen Aufbaus sind die Druckbedingungen des Vakuums, vor allem innerhalb der Glaszelle, in der die späteren Experimente im optischen Gitter durchgeführt werden sollen. Für ein stabiles Gitter wird ein Ultrahochvakuum mit einem Druck von $1 \cdot 10^{-12}$ mbar benötigt. Mit in dieser Arbeit durchgeführten Simulationen was es möglich, für den neuen experimentellen Aufbau zu zeigen, dass diese Bedingungen in der geplanten Konfiguration erreichbar sind und eine optimale Anordnung der Vakuumpumpen vorzunehmen.

Contents

1	Introduction	1
2	Atom light interactions	3
2.1	Spontaneous force	3
2.2	Doppler cooling	4
2.3	Zeeman effect	6
2.4	Magneto-optical trap	8
3	Experimental setup	13
3.1	Dysprosium	13
3.2	Experimental setup and general design considerations . .	15
3.3	Mounting of the oven section	20
4	Oven section	23
4.1	Oven setup	23
4.2	Collimation setup	24
5	Zeeman slower	31
5.1	Theory of a Zeeman slower	31
5.2	Simulation of the magnetic field	34
5.3	Atomic flight trajectories calculations	39
5.4	Construction of the Zeeman slower	40
6	Atom flux	47
6.1	Beam divergence	47
6.2	Atomic flux calculations	50
7	Vacuum simulations	55
7.1	Simulation model	56
7.2	Integrated pumping port	58
7.3	Transport tube to science cell	60
7.4	Influence of the oven	64

8 Discussion and outlook	67
A Bitter-type coil Zeeman slower	71
B Magnetic field measurements	75

List of Figures

2-1	One-dimensional optical molasses	5
2-2	Magneto-optical trap	8
2-3	Five-beam MOT	11
2-4	Capture velocity	12
2-5	Capture range	12
3-1	Dysprosium level scheme	14
3-2	Vacuum setup	16
3-3	Schematic drawing of the science cell	19
3-4	Mounting of the setup	20
3-5	CAD drawing of the mounting clamp	21
3-6	Mounting of the gate valve	22
4-1	Oven section and 2D cooling section	24
4-2	Oven crucible	25
4-3	Collimation setup for the oven	26
4-4	Heat shield comparison	26
4-5	Beam divergence of the old setup	27
4-6	Revised crucible design	28
4-7	Revised collimation setup	29
5-1	Theoretical magnetic field of the Zeeman slower	33
5-2	Simulated magnetic field	36
5-3	Difference simulated and theoretical field	37
5-4	Magnetic field slope	37
5-5	Winding plan	38
5-6	Atomic flight simulations	40
5-7	Zeeman slower mounting	41
5-8	Revised winding plan	42
5-9	Measured magnetic field	43
5-10	Difference between the simulated magnetic field and the magnetic field measured with a Hall probe.	44
5-11	Slope of the measured field	44

5-12	Zeeman slower	45
6-1	Zeeman slowe beam broadening	48
6-2	Total beam broadening	49
6-3	Temperature dependent vapour pressure	51
6-4	Transverse intensity distribution	53
7-1	Vacuum simualtion model	57
7-2	Comparison integrated pumping port - standard octagon	58
7-3	Pressure profile MOT chamber	59
7-4	Pressure profile transport tube	60
7-5	Simulation setup for different tube diameter	62
7-6	Pressure profile science cell	63
7-7	Vacuum model for the full setup	64
7-8	Pressure profile for the axis MOT chamber - science cell	65
7-9	Pressure profile for the axis pumping cross - oven	66
8-1	Current planning status	68
A-1	Bitter-type coil design	71
A-2	Simulated magentic field for the Bitter-type coil Zeeman slower	72
A-3	Inside and outside radii for the Bitter-type coil Zeeman slower	73
B-1	Measured field: suqare wire	76
B-2	Measured field: top part	77
B-3	Measured field: negative current	77

List of Tables

5.1	Adjustment of the winding parameters during the winding process	42
-----	---	----

Chapter 1

Introduction

Investigations in the field of ultracold quantum gases have resulted in evolving the understanding of atomic interactions and few-body phenomena. A major breakthrough was the creation of a Bose-Einstein condensate of Rubidium [1] and sodium [2] atoms in 1995, proving Bose and Einstein's theory of this novel state of matter, originally proposed in 1924 [3]. Over the years many more Bose-Einstein condensates of different elements have been produced, as well as degenerate fermi gases. [4].

The group of T. Pfau produced the first BEC consisting of dipolar Chromium atoms [5] in 2005. Strongly dipolar quantum gases show an interesting interplay between the isotropic, short-range contact interaction and the anisotropic long-range dipolar interaction [6, 7, 8]. A even stronger dipolar interaction has been achieved by reaching quantum degeneracy of bosonic and fermionic isotops of Erbium [9, 10] as well as Dysprosium [11, 12] due to their large magnetic moments. Dysprosium is the chemical element with the highest magnetic moment ($\mu_B = 10$), allowing an extensive investigation of the interplay of these interactions. This led to the discovery of dipolar quantum droplets in a dilute Dysprosium quantum gas [13] or to the anisotropic superfluid behavior of dipolar quantum gases [14]. Recent findings show transient supersolid properties in these dipolar quantum droplets [15, 16, 17].

To investigate the dipolar properties further a new advanced Dysprosium experiment is planned and built up at the moment in this group, featuring a spin- and energy-resolved quantum gas microscope. Resolving single Dysprosium atoms loaded into an optical near UV lattice provide the possibiliy to measure their internal properties like spin or

momentum. These kind of microscopes have been developed recently and place atoms inside an optical lattice, while imaging them with fluorescence imaging. The first quantum gas microscope was realised for alkali atoms [18], and recently also for Ytterbium [19]. Using a broad Dysprosium transition at 421 nm allows a fast imaging with a high resolution. To resolve the single atoms below the defraction limit, a narrow transition at 1001 nm in Dysprosium [20] will be used as a shelving transition. This shelving technique is inspired by imaging techniques already used in biology, like the stochastic optical reconstruction microscopy (STORM) [21, 22] or stimulated emission depletion (STED) microscopy [23]. Most atoms are excited into a long-lived state and only the few atoms left in the ground state are imaged. Afterwards the excited atoms are sequentially brought back to the ground state and imaged. For a long life time of the Dysprosium atoms in the optical lattice a very good vacuum is needed to avoid collisions with residual background atoms. Utilising this technique, the new experiment will be the first quantum gas microscope with narrow spectral resolution.

Within this thesis the first report on the design of the new quantum gas experiment is presented, focusing on the cooling mechanism for a steady source of ultracold Dysprosium atoms. Therefore a new Zeeman slower was constructed to decelerate the atoms to velocities that enables trapping them into a magneto-optical trap for further experiments. The optimised arrangement of the vacuum pumps and their pumping speed was investigated to achieve the required pressure inside the vacuum apparatus. An evaluation of the influence of the individual vacuum parts on the conductance and the pumping speed was performed.

Chapter 2

Atom light interactions

To cool and manipulate atom, understanding the interaction between the atoms and light is of great interest. This chapter summarises the theoretical foundation for understanding these interactions. The cooling mechanism using laser beams is described, as well as the trapping technique to capture the atoms. The working principle of a magneto-optical trap (MOT) using only five beams is described and first calculations for a implementation in the experimental setup are presented.

2.1 Spontaneous force

A simple model to understand atom light interaction is the Jaynes-Cummings model. It describes the coupling of a two level system to light. The electron can only occupy the ground or the excited state. If the atom is excited from the ground state into the excited state, a photon is absorbed and emitted after some time. The scattering rate of this process is then given by

$$\Gamma_s = \frac{\Gamma}{2} \frac{I/I_0}{1 + I/I_0 + (\frac{2\delta}{\Gamma})^2}, \quad (2.1)$$

where I is the light intensity, I_0 the saturation intensity, δ the detuning from the atomic transition and Γ the decay rate of the excited state. In the case of stimulated emission, the momentum of the emitted photon has the same direction as the laser beam. The total momentum transfer is zero. However in the case of the spontaneous emission, the photon can be emitted in a random direction. For a constant direction of the laser beam, the transferred momenta add up and a constant force, the so-called spontaneous force F_s , acts on the atom.

$$\vec{F}_s = \Gamma_s \Delta \vec{p} = \hbar k \frac{\Gamma I/I_0}{2(1 + I/I_0 + \frac{4\delta^2}{\Gamma^2})} \quad (2.2)$$

The resulting force on the atom points in the direction of the laser beam. For a highly saturated laser beam (in the case for $\frac{I}{I_0} \rightarrow \infty$) equation 2.2 can be simplified to

$$F_{s,max} = \frac{\hbar k \Gamma}{2}. \quad (2.3)$$

Half of the atoms populate the ground state, the other half the excited state, which results in the limited scattering force. The minimum velocity to which an atom can be cooled with the help of a laser beam is set by the recoil momentum of a photon. This minimum velocity is called the recoil velocity

$$v_{rec} = \frac{\hbar k}{m}. \quad (2.4)$$

2.2 Doppler cooling

As seen, the spontaneous light force can be used to slow down atoms and therefore cool them. Using two red detuned counter-propagating laser beams creates a one-dimensional optical molasses. For an unmoving atom the spontaneous forces of both laser beams cancel each other out, resulting in a total force of zero. If the atom moves in one direction, the Doppler effect causes it to be closer in resonance with the laser beam pointing in the contrary to the movement direction of the atom. For two counter-propagating beams with a detuning $\delta = \omega - \omega_0$ and wave vector \vec{k} , the effective detuning δ_{eff} for an atom moving with velocity \vec{v} can be written as

$$\delta_{eff}(v) = \delta_0 - \vec{k} \cdot \vec{v}. \quad (2.5)$$

The resonance is dependent on the detuning of the system and influences for which velocities the slowing process affects the atom. The detuning can be used to select a velocity class.

The spontaneous force from this laser beam acts stronger on the atom than the force from the other beam. The total force causes a slowing down of the atom. The two beams result in the forces F_+ and F_- acting

on the atom

$$\vec{F}_{\pm} = \pm \frac{\hbar \vec{k} \Gamma}{2} \frac{I/I_0}{1 + I/I_0 + \left(\frac{2(\delta \mp \vec{k} \cdot \vec{v})}{\Gamma}\right)^2}. \quad (2.6)$$

For a atom the total force then is $\vec{F}_{molasses} = \vec{F}_+ + \vec{F}_-$. For very small velocities $|\vec{k} \cdot \vec{v} \ll \Gamma|$ this term can be expanded to

$$\vec{F}_{molasses} = \frac{8\hbar k^2 \delta I/I_0}{\Gamma(1 + I/I_0 + (\frac{2\delta}{\Gamma})^2)^2} \vec{v} \approx -\beta \vec{v}. \quad (2.7)$$

The approximation is only valid for a Doppler shift smaller than the linewidth. Atoms cannot be slowed down to absolute zero velocity. The random momentum transfer only averages out for a stochastic case. Every single emission creates a random walk in momentum space with $p = \hbar k$, which results in a heating-up of the atom. The minimum temperature, the Doppler temperature T_D , is then the balanced state between the heating and the cooling process

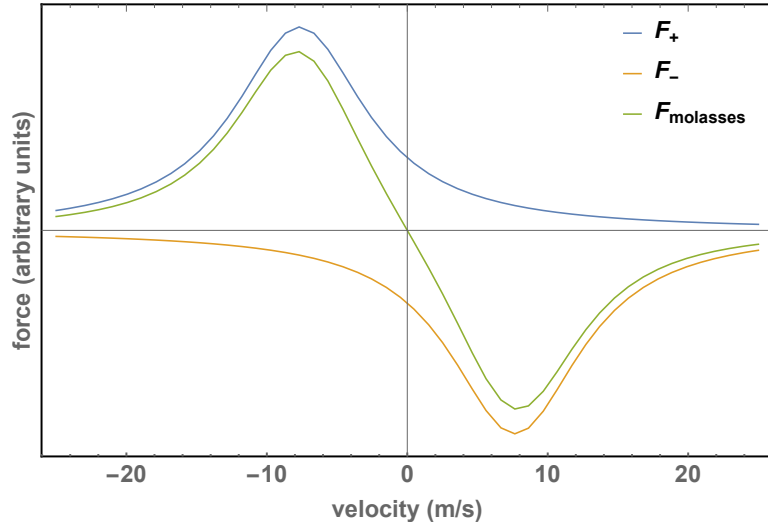


Figure 2-1: One-dimensional force acting on a optical molasses. It consists of the forces of the two counter-propagating laser beams, F_+ and F_- . A linear behaviour between the peaks can be observed. The simulation is done for two 626 nm laser beams with $I = 180I_{sat}$ and a detuning $\delta = -90\Gamma_{626}$.

$$T_D = \frac{\hbar \Gamma}{4k_B} \frac{1 + \left(\frac{2\delta}{\Gamma}\right)^2}{\frac{2|\delta|}{\Gamma}}. \quad (2.8)$$

For a detuning $\delta = -\frac{\Gamma}{2}$ this temperature is minimized

$$T_D = \frac{\hbar\Gamma}{2k_B}. \quad (2.9)$$

Cooling to the absolute zero temperature is prevented by spontaneous emission of photons, which can be compared to a heating process. The minimal temperature then corresponds to a balance between the cooling and the heating process. Further cooling can then be achieved by other means such as sisyphus cooling [24] and evaporative cooling.

2.3 Zeeman effect

One possibility to slow down atoms to low velocities and reaching low temperatures utilises the effect of an external magnetic field on the atomic energy level structure of the atoms. The influence of an external magnetic field on the energy levels can be described by the following Hamiltonian

$$H = \frac{\mu_B}{\hbar}(g_S\mathbf{S} + g_L\mathbf{L} + g_I\mathbf{I}) \cdot \mathbf{B}, \quad (2.10)$$

where \mathbf{S} is the electron spin, \mathbf{L} the orbital angular momentum and \mathbf{I} the spin of the core and g_i the responding Landé factors. The splitting of the atomic level structure into a fine structure is a result of the spin \mathbf{S} coupling to the orbital angular momentum \mathbf{L} , forming the total angular momentum $\mathbf{J} = \mathbf{L} + \mathbf{S}$ [25].

If the interaction with an external magnetic field is weaker than the hyperfine structure $\mathbf{I} \cdot \mathbf{J}$, the total angular momentum of the electron \mathbf{J} couples to the angular momentum of the core \mathbf{I} , forming the total angular momentum $\mathbf{F} = \mathbf{J} + \mathbf{I}$. F and m_F are in this case "good" quantum numbers, m_J and m_I are not. Equation 2.10 then simplifies to

$$H_{weak} = \frac{\mu_B}{\hbar}g_F F_z B. \quad (2.11)$$

For this it was assumed that the magnetic field and the quantisation axis point in the same direction, namely the z-axis. The Landé factor g_F can be written as

$$\begin{aligned}
g_F &= g_J \frac{F(F+1) - I(I+1) + J(J+1)}{2F(F+1)} \\
&+ g_I \frac{F(F+1) + I(I+1) - J(J+1)}{2F(F+1)}.
\end{aligned} \tag{2.12}$$

The Zeeman energy of an atom in a magnetic field \vec{B} is given by its magnetic dipole moment $\vec{\mu}$ and can be written in terms of the magnetic substates as

$$E_z = m_F g_F \mu_B B. \tag{2.13}$$

In a strong external field, the interaction with the magnetic field is greater than the hyperfine structure splitting. In this regime F cannot be used as a good quantum number anymore. The strong magnetic field disrupts the coupling between the orbital and the spin angular momentum. Instead J becomes a good quantum number, simplifying equation 2.10 to

$$H_{strong} = \frac{\mu_B}{\hbar} (g_J J_z + g_I I_z) \cdot B_z. \tag{2.14}$$

The corresponding Landé factor can be calculated as

$$\begin{aligned}
g_J &= g_L \frac{J(J+1) - S(S+1) + L(L+1)}{2J(J+1)} \\
&+ g_S \frac{J(J+1) + S(S+1) - L(L+1)}{2J(J+1)}.
\end{aligned} \tag{2.15}$$

For the strong magnetic field, the Zeeman shift is given by

$$E_z = \mu_B (m_J g_J + m_I g_I) B \tag{2.16}$$

For the transition frequency the Zeeman effect results in a shift δ_z between the ground state $|g\rangle$ and the excited state $|e\rangle$. For an inhomogeneous magnetic field this detuning is space-dependent. Adding δ_z to the detuning δ in equation 2.6 gives a space-dependent detuning, which can be used to compensate the Doppler shift in a Zeeman slower or a magneto-optical trap.

$$\delta_z = (g_{j,e}m_e - g_{j,g}m_g)\frac{\mu B}{\hbar} = \frac{\mu' B}{\hbar} \quad (2.17)$$

2.4 Magneto-optical trap

As seen in chapter 2.2, optical molasses can be used as an effective technique to cool atoms down to very low temperatures. But with Doppler cooling the force acts only in the velocity space. To capture the atoms, an additional spatial component of the force is needed. This can be done by using the effect of the Zeeman splitting on the different m_j states. Trapping the atoms locally can be done by adding a magnetic field to a three-dimensional optical molasses. The first magneto-optical trap (MOT) was realised by Raab et al. in 1987 [26].

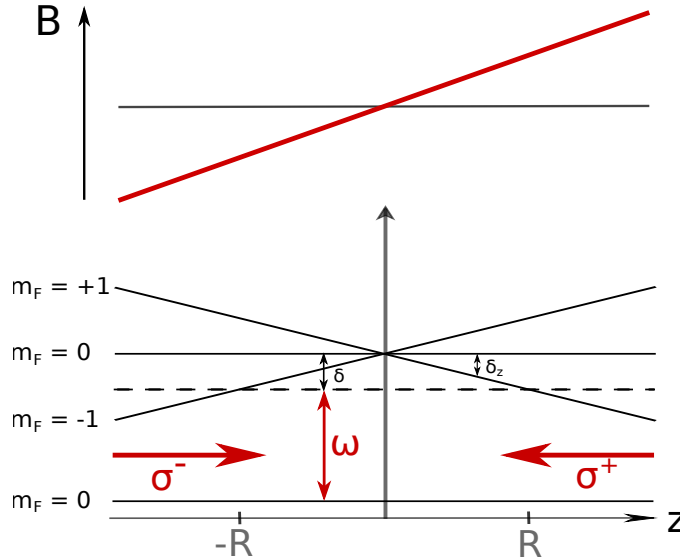


Figure 2-2: Magneto-optical trap in one dimension. The laser beams with a frequency $\omega_l = \omega + \delta$ are resonant at the positions $-R$ and R . The σ^+ polarised laser only acts on the $\Delta m = +1$ and the σ^- polarised laser on the $\Delta m = -1$ state according to the selection rules.

By applying a linear magnetic field $B_z = B' \cdot z$ generated by a pair of coils in anti-Helmholtz configuration the needed spatial dependency of the Zeeman splitting can be accomplished. The center of the trap is located at zero field ($z = 0$). In the applied magnetic field a splitting of the energy level of the atom and a linear tuning with z occurs. The magnetic field defines the quantisation axis of the atoms and is therefore flipped at $z = 0$. The $m_F = -1$ state is tuned to lower energies,

the $m_F = +1$ state to higher energies.

Two counter-propagating laser beams with σ^+ and σ^- polarisation and a red detuning $\delta < 0$ are shined in from both sides (see figure 2-2). For $\delta = 0$ the atom is in resonance with both beams in the trap center. For an atom placed at $z > 0$ the Zeeman effect shifts the $m_F = -1$ state closer to resonance and the $m_F = +1$ state away from the resonance. The two laser beams now have different scattering probabilities, where a photon from the σ^- beam is more likely to be absorbed. The atom is pushed into the trap center. Exciting atoms after passing the trap center with the σ^- beam cannot be done, because of the flipped quantisation axis the polarisation would have to be flipped as well for the beam to interact with the atoms. This prevents the beam from pushing the atoms out of the trap again. In the case of $z < 0$ the probability to scatter photons is higher for the σ^+ beam, resulting again in a force pointing towards the trap center. For $z = \pm R$ the detuning is resonance with the m_F states, marking the region in which the atoms can be captured and trapped in the MOT. The Doppler shift of the red detuned optical molasses and the Zeemans shift result in a total detuning

$$\delta_{MOT} = \delta - k \cdot v + \frac{\mu' B'}{\hbar} z. \quad (2.18)$$

The effective magnetic moment of the transition μ' is defined as the difference between the magnetic moment of the ground state $|g\rangle$ and the excited state $|e\rangle$:

$$\mu' = (g_e m_e - g_g m_g) \mu_B \quad (2.19)$$

In the experiment two coils in anti-Helmholtz configuration are used to produce the magnetic field. The field used is a rotationally symmetric quadrupole field. Typically three pairs of σ^- and σ^+ polarised laser beams generate the optical molasses.

With the spatial dependency due to the Zeeman effect added, equation 2.7 changes to

$$\begin{aligned}
\vec{F}(\vec{v}, \vec{z}) &= \frac{\hbar \vec{k} \Gamma}{2} \left(\frac{I/I_0}{1 + I/I_0 + \left(\frac{2(\delta + \vec{k}\vec{v} - \frac{\mu' B' z}{\hbar})}{\Gamma} \right)^2} - \frac{I/I_0}{1 + I/I_0 + \left(\frac{2(\delta - \vec{k}\vec{v} + \frac{\mu' B' z}{\hbar})}{\Gamma} \right)^2} \right) \\
&= -\kappa \vec{z} + \beta \vec{v},
\end{aligned} \tag{2.20}$$

with the spring constant κ of an harmonic oscillator

$$\kappa = \frac{\mu_B (g_e m_e - g_g m_g)}{\hbar k} \frac{dB}{dz} \beta = \frac{\mu'}{\hbar k} B' \beta. \tag{2.21}$$

The capture range z_c of a MOT is defined as the region between $-R$ and R , where the force (see equation 2.20) can push the atoms back.

$$z_c = \frac{\hbar |\delta|}{\mu' B'} \tag{2.22}$$

The trapping behaviour is also dependent on the velocity of the atoms. Typical capture velocities for a MOT are between 5 m/s to 40 m/s. Therefore atoms need to be slowed down, for example with the help of a Zeeman slower or cryogenic buffer gas. The target capture velocity for the narrow-line MOT is 8 m/s. To estimate the maximum capture velocity v_c the maximum energy of a atom entering the MOT at $z = -R$ and slowed down to standstill at $z = R$ can be calculated. From the energy then the capture velocity evaluated.

$$v_c = \sqrt{\frac{2\hbar^2 |\delta| k \Gamma}{\mu' B' m}} \tag{2.23}$$

In the new setup, a special version of a MOT will be used. Due to the heavy atomic mass of the Dysprosium atoms, gravitational force is large enough to replace one of the beams on the z-axis. This so-called five-beam MOT was at first realised in the Innsbruck experiment [27]. A great advantage of this setup is the free viewport, giving space to additional optical access, for example for imaging. A schematic of the

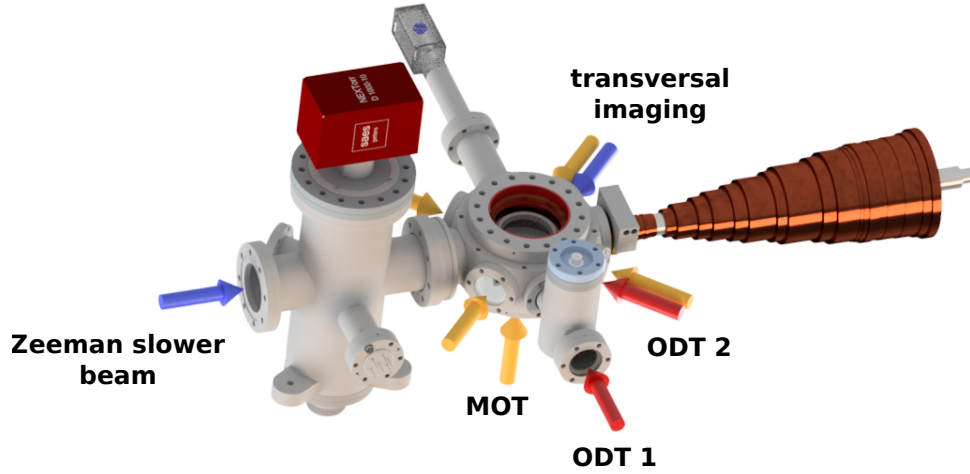


Figure 2-3: Schematic of the five-beam MOT. Shown in orange are the five MOT beams, in blue a transverse imaging beam. Two optical dipol traps (red) can be used to trap and transport the atoms.

MOT beam configuration is shown in figure 2-3.

To capture atoms inside the MOT, a narrow-line transition at 626 nm with a linewidth of $2\pi \cdot 136$ kHz is used. Vertical MOT coils are set into the recessed bucket viewports, producing the magnetic gradient field of $B' = 3$ G/cm. The recessed bucket viewport ontop allows a direct mounting of an objective as near as possible to the MOT. With a chosen detuning of $\Delta = -50$ Γ and a saturation factor of $I_{626} = 160 \cdot I_{sat}$ ($I_{sat,626} = \pi\hbar c\Gamma_{626}/3\lambda^3 = 72$ $\mu\text{W}/\text{cm}^2$), the capture velocity of the MOT is estimated to 8 m/s and a capture radius of 0.96 cm (see figure 2-5).

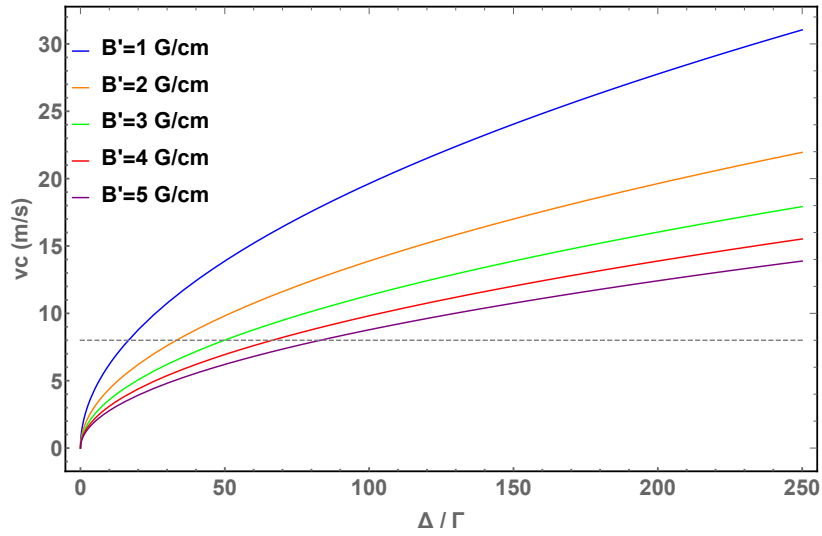


Figure 2-4: Capture velocity v_c as a function of the detuning of the MOT beams for different magnetic field gradients. For a target capture velocity of 8 m/s, this yields a detuning of $50 \cdot \Gamma_{626}$ for 3 G/cm.

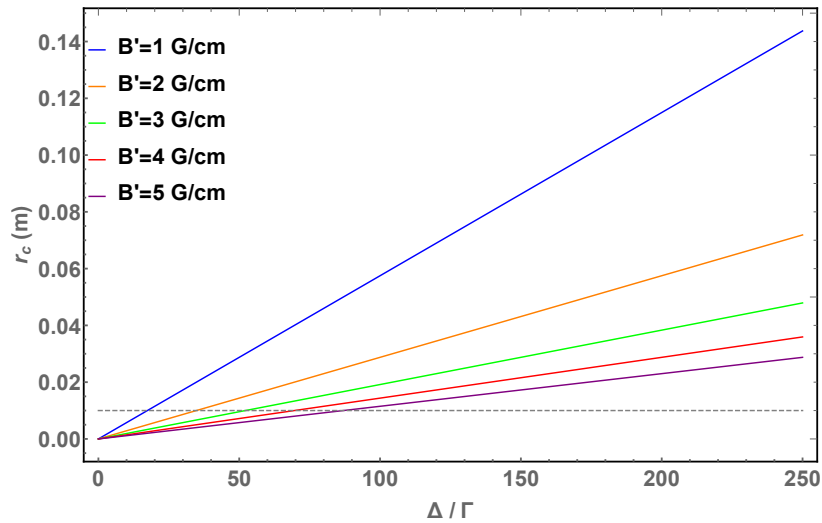


Figure 2-5: Capture range r_c as a function of the detuning of the MOT beams for $\Gamma_{626} = 136$ kHz for different magnetic field gradients. The intended capture radius of 1 cm is marked by the dashed grey line. For $B'=3$ G/cm this again results in a detuning of $\delta = 50 \cdot \Gamma_{626}$.

Chapter 3

Experimental setup

The topic of this chapter is the design of the Dysprosium quantum gas microscope. It will allow a single site resolution of Dysprosium atoms inside an optical lattice. A general overview over the new experimental setup is given, focussing on the vacuum and cooling sections. Mounting the system and general design considerations are discussed as well.

3.1 Dysprosium

The element, that will be used in the experiment is Dysprosium, a rare-earth element in the lanthanide group. It was first discovered in a Holmium sample in 1886 by the french chemist Paul-Emile Lecoq [28]. Prior to this, the two elements were thought to be one substance. The name (from the greek word dysprositos: "hard to get at") illustrates the difficulty to separate Dysprosium and Holmium.

Dysprosium consists of 66 protons and electrons and occurs naturally in four stable isotops. Of the four, two of these are bosonic, ^{162}Dy (25.48 %) and ^{164}Dy (28.26 %), the other two, ^{161}Dy (18.89 %) and ^{163}Dy (24.90 %), are fermionic [29]. Dysprosium has a high melting point of 1407 °C and a boiling point of 2600 °C.

The ground state configuration of Dysprosium is $[\text{Xe}]4f^{10}6s^2$, leading to a partly filled 4f-shell and a filled 6s-shell. The missing electrons in the 4-shell result in an angular momentum of $\mathbf{L} = 6$ and a total electron spin of $\mathbf{S} = 2$, leading to a total angular momentum of $\mathbf{J} = 8$. In the term formalism the ground state can be written as $^5\text{I}_8$. The nuclear spin for the fermionic isotops is $\mathbf{I} = 5/2$, which causes a splitting in six hyperfine states, $\mathbf{F} = 11/2$ to $\mathbf{F} = 21/2$. For the bosonic isotops no

hyperfine splitting is observed.

Dysprosium is, along with Terbium, the element with the highest magnetic moment of $\mu_m = 9.98 \mu_B$, due to its high angular momentum. This high magnetic moment opens a new field in the investigation of quantum gases, using the strong dipolar interaction.

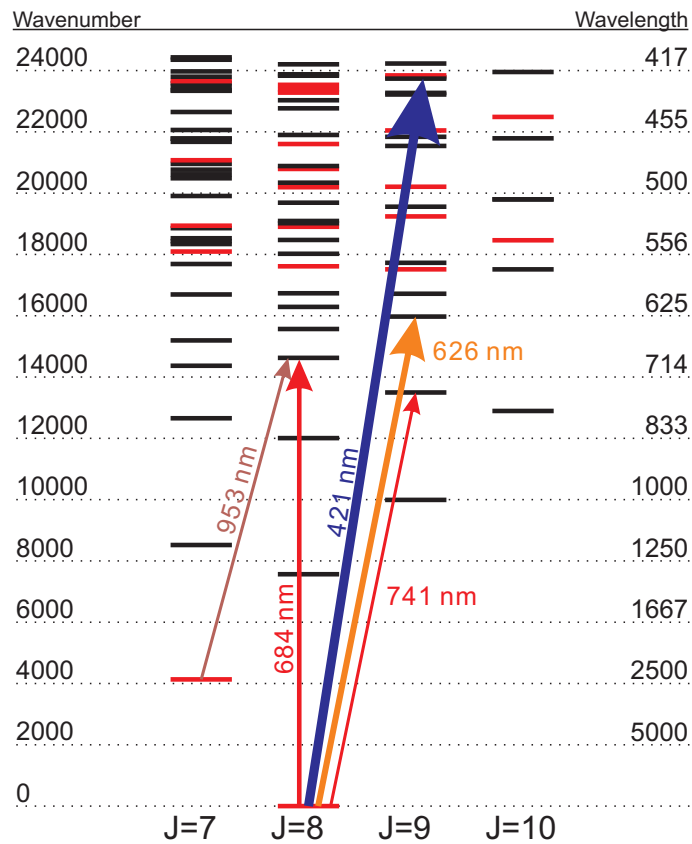


Figure 3-1: Level scheme for Dysprosium with some of the used transitions.

Cooling Dysprosium to degeneracy

To generate Dysprosium gas, high purity granulate (99.9 %) is heated up inside a crucible in an effusion cell to temperatures of $T=1250 \text{ }^\circ\text{C}$. The oven is mounted inside a vacuum system, with a pressure of $p \approx 10^{-9}$ mbar. Under these conditions, the atoms are sublimated and leave the oven through a small aperture. To focus the atomic beam and cool the atoms in the transverse direction, a transversal cooling scheme using the red detuned light of the 421 nm transition is utilised. The mean

velocity in the longitudinal direction of the atoms is with around 450 m/s to fast to directly trap atoms in a magneto-optical trap. Using a spin-flip type Zeeman slower working also on the 421 nm transition, the atoms are decelerated to 8 m/s and then trapped inside a magneto-optical trap.

Atoms leaving the Zeeman slower and entering the MOT chamber are captured in a narrow-line magneto-optical trap operating at 626 nm with a linewidth of $\gamma = 136$ kHz. To increase the number of captured atoms, large trapping beams with a high intensity are used. The laser line width is increased with the help of a spectral broadener to increase the velocity range and the captured number of atoms further [27]. Atoms can be loaded into the MOT with a temperature of around 500 μ K [30]. Reducing the temperature is done by compressing the MOT. This is done by reducing the detuning and intensity of the 626 nm trapping beams. A temperature of 6 μ K is reached, which is enough to load the atoms into an optical dipole trap.

To reach lower temperatures and achieve quantum degeneracy, evaporative cooling is used to cool the atoms further. The hottest atoms are removed by lowering the depth of the trapping potential. If the decrease takes place slow enough, the atoms can rethermalise through two-body collisions, resulting in lower mean temperature of the remaining atoms. A Dysprosium Bose-Einstein condensate with a temperature of 50 nK can be created by decreasing the intensity of the trapping beams.

3.2 Experimental setup and general design considerations

The experimental apparatus, shown in figure 3-2, consists of four important parts: The oven chamber, the cooling section, the MOT chamber and the science cell. The Zeeman slower works as a differential pumping stage, which is used to separate two different pressure regions, the high vacuum section ($p \approx 10^{-8}$ mbar) in the oven and cooling section and the UHV¹ section ($p \approx 10^{-11}$ mbar) in the MOT chamber and the science cell. The high vacuum in the science cell is needed to prevent collisions between the Dysprosium atoms and the residual background gas.

¹UHV: ultra-high vacuum

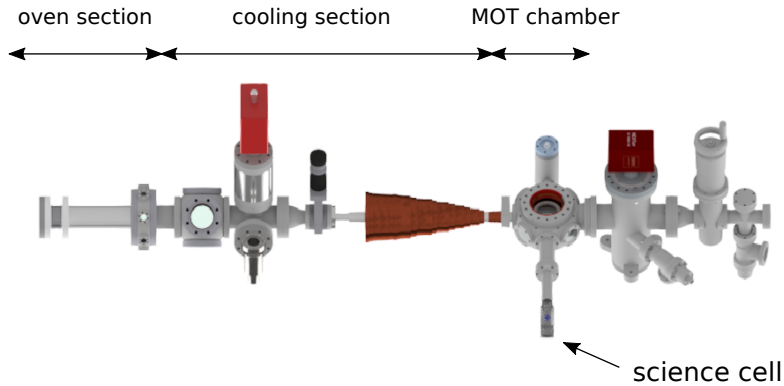


Figure 3-2: Schematic drawing of the vacuum setup. The apparatus consists of four main parts: The oven chamber, the cooling section, the MOT chamber and the science cell.

During the design of the new experimental setup, several requirements occurred, which had to be taken into account. Not only optical accesses of the different laser beams have to be considered, but also the geometry of the setup, when designing the vacuum part. The use of standard parts reduces the time setting up the experimental setup. The experimental setup can be divided in several subparts. Each section has requirements which have to be considered while designing the new experimental setup.

A strong limitation on the whole setup is the limited size of the optical table. For the optical table a size of 2.4 m x 1.5 m was chosen. This limits primarily the length of the vacuum setup. The 421 nm cooling laser has to pass through the whole experimental setup. The strongest effect is on the Zeeman slower. While a longer Zeeman slower results in a larger security factor, a length of around 1 m like in the current setup would be impractical. For a shorter Zeeman slower, smaller deviations of the magnetic field from the ideal case have to be heeded.

For the future experiments, which are very susceptible to fluctuating magnetic fields, inside the science cell a high magnetic field stability is required. Therefore a mu-metall shielding will be designed around the cell. This will take a significant amount of space around the cell, limiting the optical access on the viewports at one side of the MOT chamber.

Another issue, which has to be considered during the design process,

are the demands on the vacuum pressure. For a stable lattice inside the science cell, a very good ultra-high vacuum with a pressure on the order of 10^{-12} mbar will be needed. Placement and pumping speed of the used vacuum pumps have to be considered carefully. In the MOT chamber a pressure of 10^{-11} mbar is required, while in the transversal cooling section only 10^{-9} mbar is sufficient. To separate the two pressure regions, the Zeeman slower can be used to act as a differential pumping stage. Pumping speed and positioning of the vacuum pumps are simulated to control, if these requirements are fulfilled. A detailed description can be found in chapter 7.

Oven chamber

Dysprosium is heated up inside the effusor cell (EC) of the oven² to a temperature of around 1200 °C. The adjoining hot lip (HL) can be heated with a higher temperature of 1250 °C to prevent condensation on the aperture. Two apertures are used to collimate the atomic beam. A heat shield is added at the opening of the oven and EC and HL are inside a water cooled cylinder.

The new design of the crucible shows a large angle of emergence when used in the current Dysprosium experiment. To prevent a large loss of atoms and coating of the experimental setup, especially the viewports of the 2D cooling, further steps to collimate the atomic beam have to be taken into account. This collimation will be done by adding an additional aperture after the opening of the oven. In addition, the design of the crucible was revisited.

A shutter is included in the oven design to block the atomic beam. To have enough space for a shutter to block the atomic beam, the oven is mounted on a separate oven chamber. A direct mounting of the oven into the 2D cooling chamber is not possible, as no additional beam collimation could be incorporated into the design. By the means of small viewports on the oven chamber, beam spectroscopy can be done directly at the oven opening.

2D-cooling section and Zeeman slower

The cooling section consists of two parts: The transversal cooling and the Zeeman slower. Atoms leave the oven under a large angle of emergence. With the help of an aperture between the oven chamber and the

²CreaTec Fischer & Co. GmbH

2D cooling chamber diverging atoms are cut out to prevent a coating of the experimental apparatus. Otherwise most of the atoms will hit the walls of the Zeeman slower tube and are lost for experimental purposes. Large elliptical beams of the 421 nm light with a detuning of $\Delta = -1\Gamma_{421}$ slow down the atoms in their transversal velocity by optical access in two orthogonal directions. The laser beams will be widened from 2-3 mm to 6 cm to cover a large overlap with the atomic beam for the transversal cooling of the Dysprosium atoms. The atomic beam is collimated, so the atoms do not diverge while travelling through the Zeeman slower tube.

In the Zeeman slower the longitudinal velocity of the Dysprosium atoms is slowed down from 645 m/s to 8 m/s to allow the atoms to be trapped inside the narrow-line MOT. The Zeeman slower is not directly mounted on the tube between the 2D cooling and the MOT chamber, but on a separate tube. This guarantees not only that no stress acts on the tube flanges, but also that a position adjustment of the Zeeman slower is possible after assembling the setup. The high currents used to generate the magnetic field of the Zeeman slower produce a lot of heat. To prevent damage of the wire and the insulation, the wires have to be water-cooled. The thick wire, which makes up the bulk part of the Zeeman slower is internally water-cooled, using a hollow core wire. The second type of wire has to be cooled externally in the regions with high currents.

MOT chamber

After passing through the Zeeman slower, the atoms have a longitudinal velocity of 8 m/s and reach the MOT region, where they are caught. To reach the needed UHV, a large ion getter pump³ with a pump speed of 1000 l/s is mounted near the MOT chamber. While a direct mounting would result in an increased pumping speed, the large viewports of the chamber are needed for optical access for the MOT and imaging. With an integrated pumping port an increased conductivity and therefore effective pumping speed is assured. An additional small getter pump⁴ is mounted on the axis of the transport beam. Due to the heavy atomic mass of Dysprosium, only five beams are needed for the MOT [27]. The free viewport can then be used for mounting an objective directly from the top. Also optical access for two optical dipole traps (ODT) is

³SAES NEX Torr D1000

⁴SAES Capacitor Z200

included in the design of the MOT chamber. One ODT will be used for the optical transport inside the science cell. Evaporative cooling can be done already inside the MOT chamber with the second crossed ODT under a 45° angle.

Science cell

The atoms trapped inside the MOT will then be transported with an optical dipole trap (ODT) into the science cell. The glass cell is made out of fused silica and coated for 362 nm. On top of the cell a hemisphere is optical contacted, acting as a solid immersion lens [31]. This approach allows a resolution below the Abbe limit. The atoms are then loaded into a UV lattice with a wavelength of 362 nm.

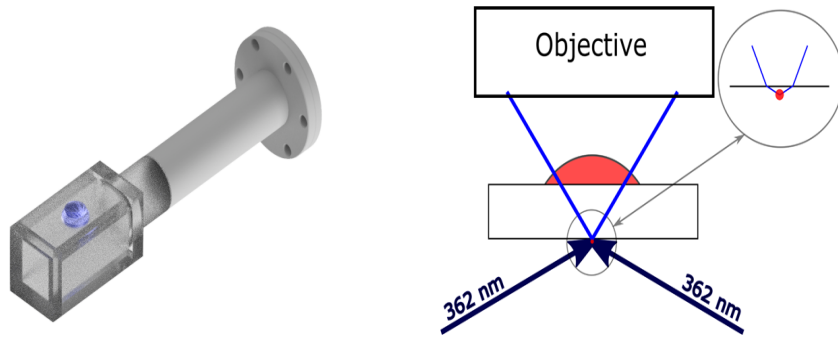


Figure 3-3: **Left:** CAD drawing of the science cell. The hemisphere is shown in blue. **Right:** Schematic drawing of the accordion lattice and the imaging principle [31].

Transporting the atoms from the MOT chamber to the science cell will be done via a ODT where the last lens is on a translation stage. This limits the transport length to 40 cm, fixing the length of the transport tube to the science cell. Also the proximity of the magnetic shield towards the MOT chamber is affected.

As mentioned before, magnetic field control near the science cell will be important for the design approach. Not only the placement of compensation coils is significant, also the positioning of the vacuum pumps. Large traditional ion pumps produce a strong magnetic stray field. The pumps chosen for the new setup will be consisting of a passive pumped NEG element with only a small ion pump, reducing the overall stray

fields. Another advantage of this kind of pumps is their compact design and low weight. Additionally no pump can be placed between the science cell and MOT chamber. A magnetic stray field at this position could strongly affect the shielding ratio of the magnetic shielding and is limited by spatial restrictions.

3.3 Mounting of the oven section

For a stabile mounting of the experimental setup, a rack made out of aluminium profile⁵ with a edge length of 30 mm and 40 mm was used. The end of the Zeeman slower pointing towards the MOT chamber is additionally mounted on a single pillar (see figure 3-4). Due to limited space no large rack can be used at this position. The large part of the Zeeman slower is then mounted on an aluminium rack, which bears most of its weight.

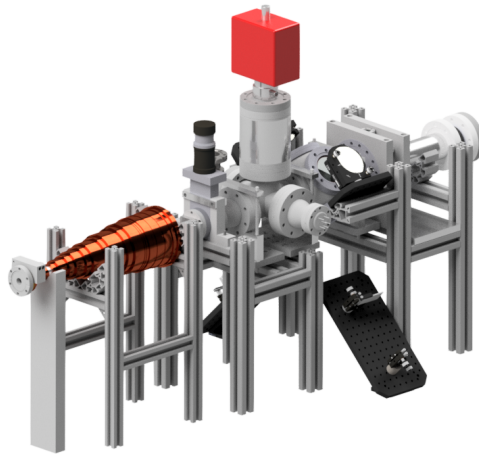


Figure 3-4: Mounting of the 2D cooling section and the Zeeman slower. The rack is made out of Rose+Krieger profiles.

The 2D cooling section is mounted on a separate rack. Since the cube has no holes, which can be used to mount any pillars directly, a different approach was used. On the flange connecting the oven chamber and the cube and on the five-way cross clamps (see figure 3-5) are mounted onto the rack to fix the orientation of the setup along its axis,

⁵Rose+Krieger, PROFILE TECHNOLOGY BLOCAN

as well as its height. Other positions used to hold the setup in place are the flanges of the oven chamber and the gate valve. The flanges are enclosed in separate pillars, holding them into place. The gate valve meanwhile has again no intended mounting holes. Two L-shaped bars pressed against the valve are used to fix the valve position. Additional small bars press the L-shaped bars together and prevent a tilt of the valve in the other direction. A CAD drawing of the valve mounting is shown in figure 3-6.

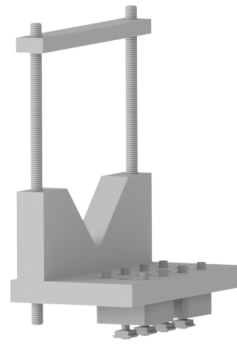


Figure 3-5: CAD drawing of the clamp used to hold the five-way cross and the flange at the 2D cooling chamber in place.

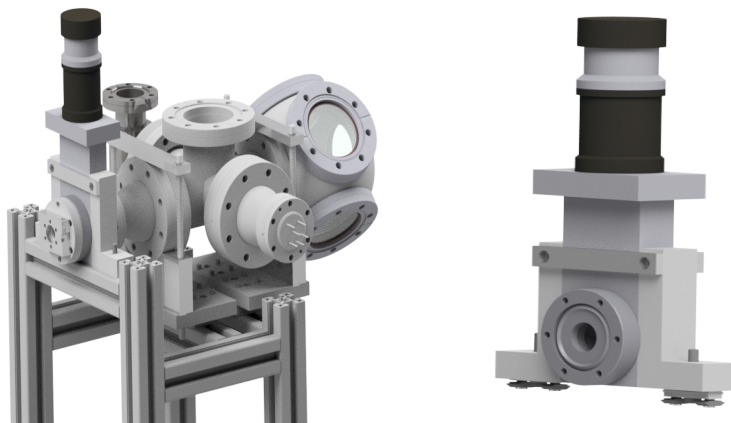


Figure 3-6: **Left:** Mounting of the gate valve connecting the ZS and the 2D cooling section. The L-shaped bars hold the valve in place **Right:** Detailed view of the gate valve mounting.

Chapter 4

Oven section

Dysprosium naturally occurs in a solid form, however for most of the experiments in atomic physics atoms are needed in their gaseous form to achieve a high atomic flux. The atoms are heated up inside an effusion cell to temperatures around 1250 °C to get them into the gaseous phase, leaving the oven under a large diverging angle. For a better beam collimation, a transversal cooling stage and a special design of the effusion cell is needed and was included in the new experimental setup.

In this chapter, the built-up of the oven section will be described. A new dual-filament effusion cell is used to produce a beam of Dysprosium atoms. Furthermore a setup to collimate the atomic beam is presented.

4.1 Oven setup

For loading the atoms from an oven into a MOT, the oven has to be mounted directly into the vacuum. For refilling the crucible, the oven needs to be separated from the rest of the vacuum system so that the high vacuum is preserved. Separating the oven section from the rest of the vacuum setup is done with the help of a valve. That way only the oven section has to be pumped, leaving the vacuum in the science cell and MOT chamber undisturbed. In addition optical access for the transversal cooling near the opening of the oven has to be included. A schematic drawing of the oven section is shown in figure 4-1.

In the former experiment the opening of the oven used was blocked over time due to the condensation of Dysprosium atoms at the cold water cooling unit. To prevent condensation and increase the beam

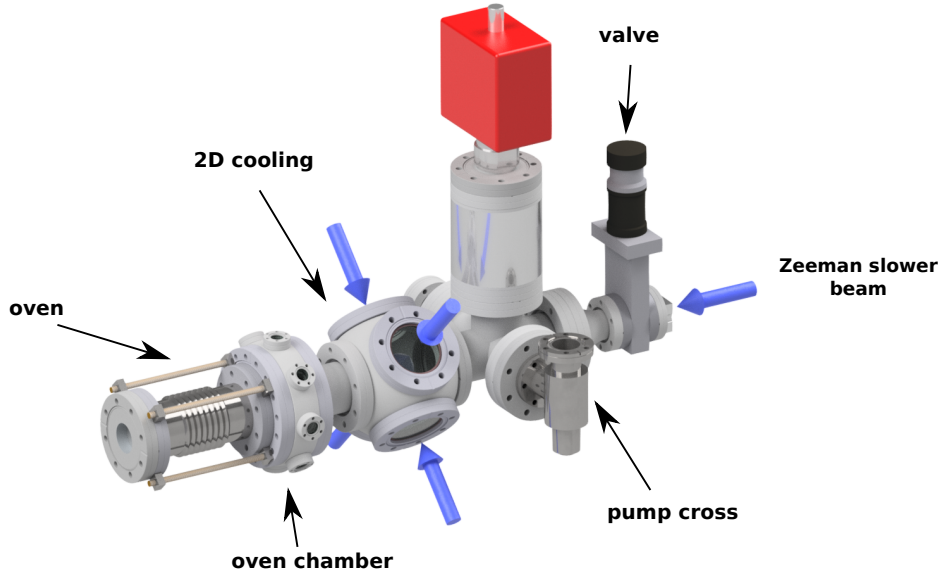


Figure 4-1: CAD drawing of the oven and the 2D cooling section. The oven (right) is mounted in a separate chamber from the 2D cooling chamber. On the right is the gate valve connecting the 2D cooling section to the Zeeman slower.

collimation of the atomic beam leaving the oven, a new effusion cell was designed for the new experiment. The effusion cell used was manufactured by the company CreaTec Fischer & Co. GmbH¹. It is separated into two different regions, the effusion cell (EC) and the hot lip (HL). Due to the large temperatures needed to evaporate Dysprosium, the crucible of the effusion cell is made out of molybdenum. Inside the effusion cell, Dysprosium granulate is heated up. A large filling volume of around 50 g guarantees a long working time². The adjacent hot lip can be operated at a 50 °C higher temperature than the effusion cell, preventing material condensation at the water-cooled heat shield. Two apertures in the HL collimate the atomic beam. A schematic drawing of the crucible is shown in figure 4-2.

4.2 Collimation setup

Following [32] the number of atoms dN leaving the oven into a region $d\Omega$ within the time interval dt through an aperture with diameter A under

¹Effusion cell DFC-40-25-285-SHE-Col

²filling volume old crucible version: around 8 g

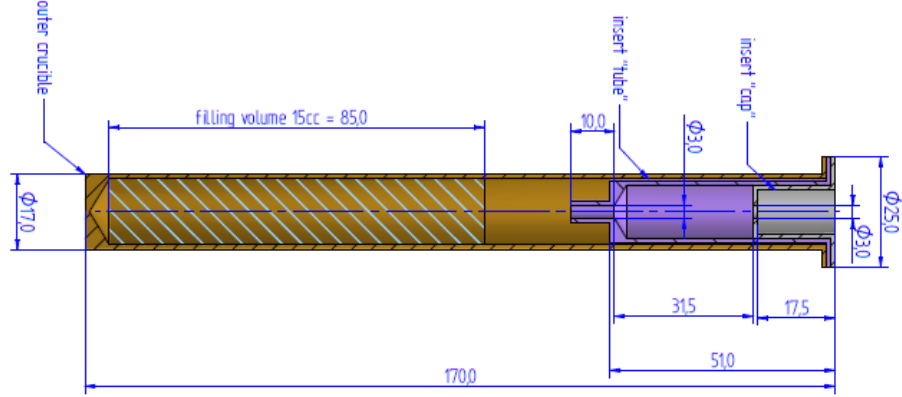


Figure 4-2: Schematic drawing of the oven crucible. For better beam collimation and to prevent condensation, the crucible is separated in an effusion cell and a hot lip (purple).

an angle α (see figure 4-3) with a mean velocity \bar{v} can be expressed as

$$dN = \frac{d\Omega}{4\pi} n \bar{v} \cos \alpha A dt, \quad (4.1)$$

where n the atomic density. Maximising the atomic flux at the position of the MOT is needed for a high atom number and faster loading times. A small angle of emission is required in the experiment, since only these atoms can travel through the setup without hitting a wall and getting lost for experimental purposes. To decrease the emission angle, a second aperture can be added, generating a directed beam by cutting off the unused part of the atomic beam. For the first aperture to work, atoms should not accumulate in the HL. Otherwise it would exhibit an oven-like behaviour such as the EC. To prevent condensation on the aperture and a consequential overgrowth, the apertures are heated and potential condensed atoms are reemitted.

The atoms leave the oven under an angle α (figure 4-3) into a solid angle Ω around the z-axis

$$\Omega = 2\pi(1 - \cos(\alpha)), \quad (4.2)$$

with $\alpha = \arctan(f)$ and the collimation ratio $f = \left(\frac{b_1/2+b_2/2}{a}\right)$. After a distance l the beam has diverged to a diameter d

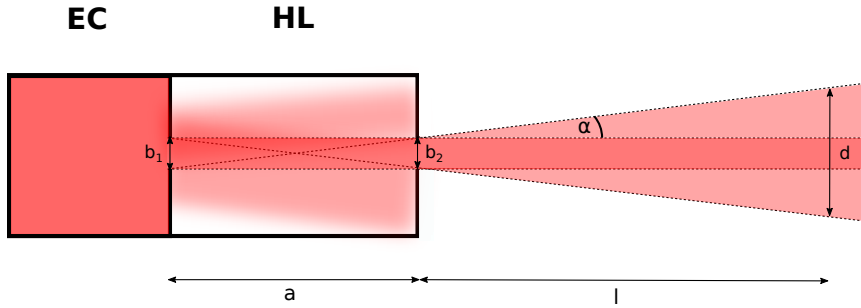


Figure 4-3: Schematic drawing of the oven collimation using two apertures [32]. The aperture with diameter $b_1 = b_2 = 3$ mm are $a = 31.5$ mm apart. The beam is broadened after $l = 50$ mm to $d = 11.6$ mm.

$$d = 2 \left((a + l)f - \frac{b_1}{2} \right). \quad (4.3)$$

For the oven values given in figure 4-2 a beam broadening of 11.6 mm after a 50 mm distance from the second aperture can be calculated. The angle of emission is expected to be 0.023° .

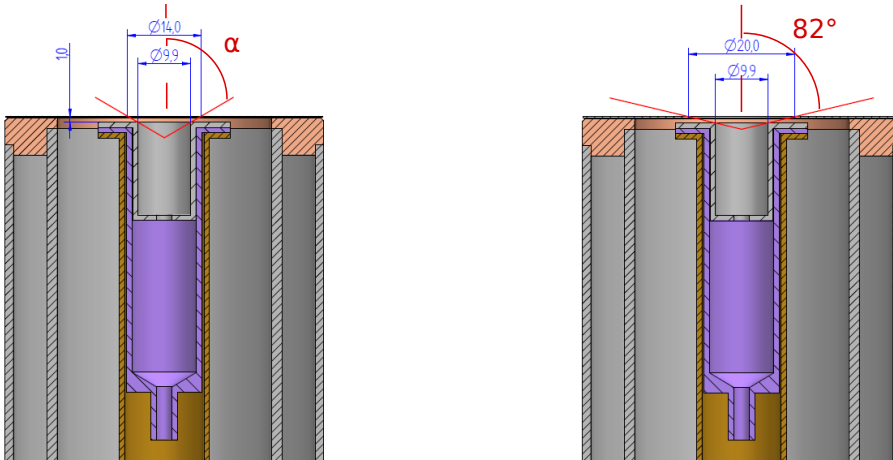


Figure 4-4: Comparison of old version (left) of the heatshield the with the new design (right). Increasing the aperture diameter from 14 mm to 20 mm is supposed to prevent condensation and guarantee a longer operating time.

The running experiment at the already existing setup with the dual-filament effusion cell shows, that the collimating principle of the two apertures does not work as intended. Instead of a collimated atomic beam, the oven emits the atoms under a large angle, resulting in a

partial coating of the 2D cooling viewports (see figure 4-5). From the positioning of the coating, a angle of emission of 82° was estimated. A reason for this could be, that the vapour pressure in the hot lip is the same as in the effusion cell, rendering the first aperture useless. Therefore the beam becomes collimated by the second aperture and the insert cap, which acts as an effective aperture with a diameter of 9.9 mm. Another factor could be the new design of the heat shield, see figure 4-4. The diameter of the heat shield was increased to prevent condensation, which limited the operation time in previous iterations. The schematic drawing includes in red an maximum angle, which approximately corresponds to the observed angle of emission. From this it seems that the angle is only given by the heat shield, not the apertures of the crucible.

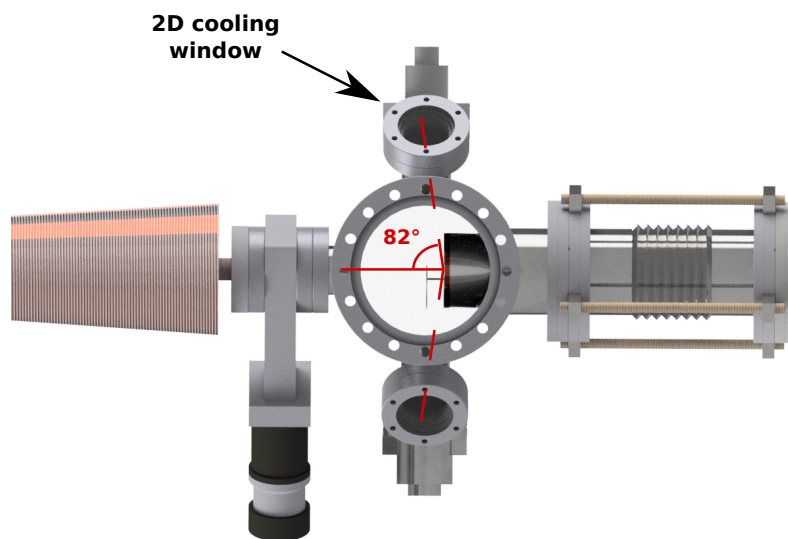


Figure 4-5: Divergence of the atomic beam in the existing experiment. The atoms leave the oven under a large angle of 82° and coat the viewports for the transversal cooling.

To solve this problem, the atoms have to enter the 2D cooling chamber under a smaller angle, but condensation at the opening of the oven should be prevented to ensure a longer operation time. Therefore a simple simulation³ was done to control the influence of the emission

³Molflow+ Version 2.6.70

angle on the new setup. A Monte-Carlo simulation of the trajectories of atoms leaving the oven was performed. For simplicity every atom outside the oven hitting a wall was absorbed. Counting the atoms hitting the viewport surfaces compared to the total atom number leaving the oven gives an indication, how strong the influence is. In total 28 % of the atoms leaving the oven ended up on the viewport areas. Coating of the viewports will ruin the advantage of the large CF63 viewports for using large transversal cooling beams. Mounting the oven directly into the transversal cooling chamber therefore is not a possibility.

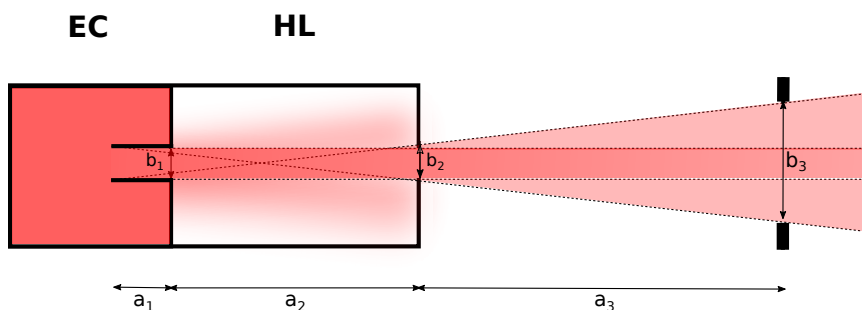


Figure 4-6: Revised crucible design for a more collimated atomic beam. A third aperture is added after a distance a_3 . On the first aperture a tube with length a_1 is added to separate the different vapour pressure regions of EC and HL [32].

A solution to this problem is to add a third aperture between oven and transversal cooling chamber. This aperture cannot be heated like the other two inside the effusion cell, which are a part of the crucible. Therefore a larger diameter has to be chosen to prevent condensation of atoms blocking the aperture. Adding a longer tube to the first aperture should also increase the beam collimation by better separating the EC and HL region. A schematic drawing of the revised collimation setup is shown in figure 4-6.

Due to the extra space needed between the third aperture and the end of the effusion cell, the oven cannot directly be placed inside the 2D cooling chamber as done before. For opening and closing the oven shutter additional space is needed. Without an option to block the atomic beam, atoms from the oven would collide with atoms loaded into a MOT or ODT. Blocking the beam ensures a long lifetime of experiments inside the MOT chamber. A separate chamber⁴ for the oven

⁴Kimball Physics 6" spherical octagon, thin version

is included in the setup, connected to the 2D cooling chamber by a tube with an additional aperture with a 22 mm diameter . This setup is shown in figure 4-1.

A detailed view of the revised version of the collimation setup is shown in figure 4-7. The third aperture is placed 122 mm away from the oven opening. Using equation 4.3 to calculate the spread at the position marked, gives a beam diameter of 37 mm. This position lies 215 mm away from the oven opening and marks the first spot where atoms can hit the viewport. The calculation shows that for this diameter no coating of the viewports will occur in the experiment. Trajectory simulations confirm, that for the new configuration atom cannot hit the viewport surfaces.

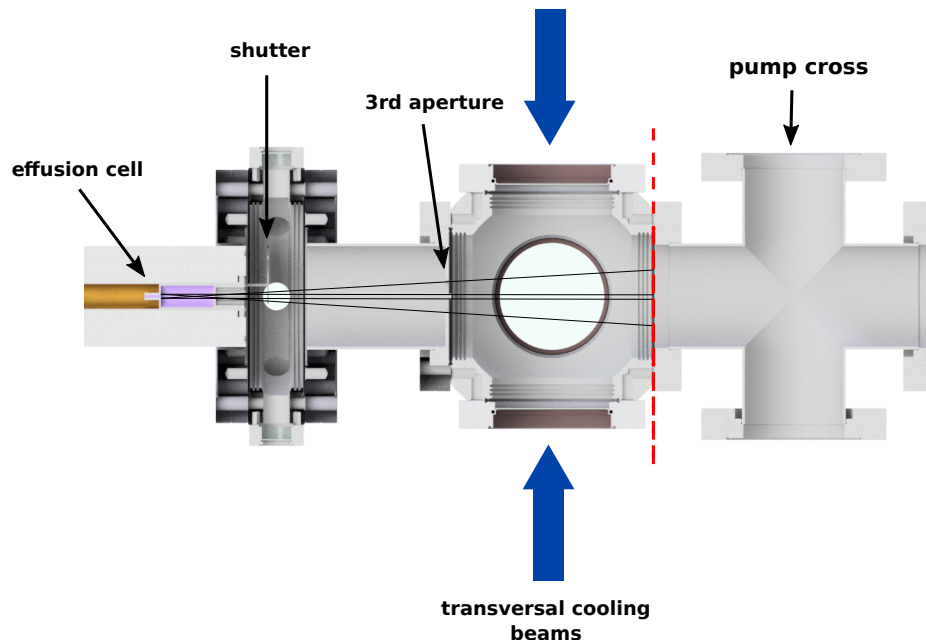


Figure 4-7: Schematic drawing of the revised oven collimation setup. A third aperture with a diameter of 22 mm is placed in front of the 2D cooling chamber. The separate oven chamber for the shutter can be seen on the left. At the marked position (red) the atomic beam diameter is 37 mm.

Chapter 5

Zeeman slower

Atoms leaving the oven with a high velocity cannot directly be trapped inside a magneto-optical trap (MOT). With the help of a Zeeman slower and laser cooling [33] this problem can be overcome. Using the Zeeman shift to compensate for the Doppler effect, atoms can be cooled down to ultracold temperatures, allowing the loading of a large number of atoms into a MOT.

This chapter discusses the development of the Zeeman slower for the new Dysprosium experiment. The working principle of a Zeeman slower is introduced, as well as the simulation of the magnetic field of the Zeeman slower. At last the construction process is presented.

5.1 Theory of a Zeeman slower

Atoms leaving the oven have a velocity profile in form of a modified Boltzmann distribution. Therefore their mean velocity for oven temperatures around 1400 K is higher than the capture velocity for trapping in a MOT ($v_{c,MOT} = 8$ m/s). Only a small portion of the atom beam can directly be trapped. With the use of a Zeeman slower the number of trapped atoms can highly be increased. The Zeeman shift is used to compensate the Doppler effect during the deceleration process. As the Doppler effect changes with the deceleration of the atoms, a space dependent magnetic field is used to adjust the Zeeman shift during the flight. Using photon scattering, atoms entering the Zeeman slower with a velocity lower than the capture velocity v_c of the ZS are slowed down to a final velocity v_f .

The maximum deceleration on an atom induced by radiation force

(equation 2.1) is

$$\begin{aligned}
 a &= \frac{F_s}{m} = \frac{\hbar k}{m} \Gamma_s(I_{sat}) \\
 \Rightarrow a_{max} &\stackrel{I_{sat} \rightarrow \infty}{=} \frac{\hbar k}{m} \frac{\Gamma}{2}.
 \end{aligned} \tag{5.1}$$

With the help of an inhomogeneous magnetic field along the z-axis, one can counter the varying Doppler shift $\delta_{Doppler} = \vec{k} \cdot \vec{v}$. The magnetic field shifts the different atomic levels due to the Zeeman effect depending on the spatial position. This results in an effective detuning of

$$\delta_{eff}(z) = \delta_0 + \delta_{Doppler} + \frac{\mu' B(z)}{\hbar} \tag{5.2}$$

where $\delta_0 = \omega - \omega_0$ is the initial detuning of the cooling laser. μ' is difference of the magnetic moments of the ground and the excited state ($\mu' = (g_e m_e - g_g m_g) \mu_B$). For the laser cooling of the Dysprosium atoms the broad $J = 8 \rightarrow J' = 9$ transition with a wavelength of 421 nm and a transition rate of $\Gamma = 2\pi \cdot 32.2$ MHz. is used ($6s^2(^1S_0) \rightarrow 6s6p(^1P_1^0)$ [34]). The ground state has a magnetic quantum number $J_g = 8$ and a Landé factor of $g_g = 1.24$, the excited state $J_e = 9$ and $g_e = 1.22$ [35].

Assuming a constant acceleration during the flight through the Zeeman slower, the velocity of an atom for a position z is given by

$$v(z) = v_c \sqrt{1 - \frac{z}{l_0}}. \tag{5.3}$$

Here v_c is the capture velocity of the Zeeman slower and l_0 the length needed to reduce the atom to a final velocity v_f :

$$l_0 = \frac{(v_c)^2 - v_f^2}{2a_{max}} \tag{5.4}$$

The magnetic field $B(z)$ for slowing the atoms can be obtained by combining equation 5.2 and 5.3. For a maximum acceleration one gets the following field:

$$B(z) = B_{bias} + B_0 \sqrt{1 - \frac{z}{l_0}} \tag{5.5}$$

Where B_{bias} is the magnetic bias field

$$B_{\text{bias}} = \frac{\hbar\delta_0}{\mu'} \quad (5.6)$$

and B_0 the height of the magnetic field change

$$B_0 = \frac{\hbar kv_c}{\mu'} \quad (5.7)$$

Because a Zeeman slower can not be wound perfectly and therefore to ensure, that the resonance condition (equation 5.2) is not violated, a security factor $s_f = 0.87$ for a lower the acceleration is added in the equations [35]:

$$a_{zs} = 0.87 \cdot a_{max} \quad (5.8)$$

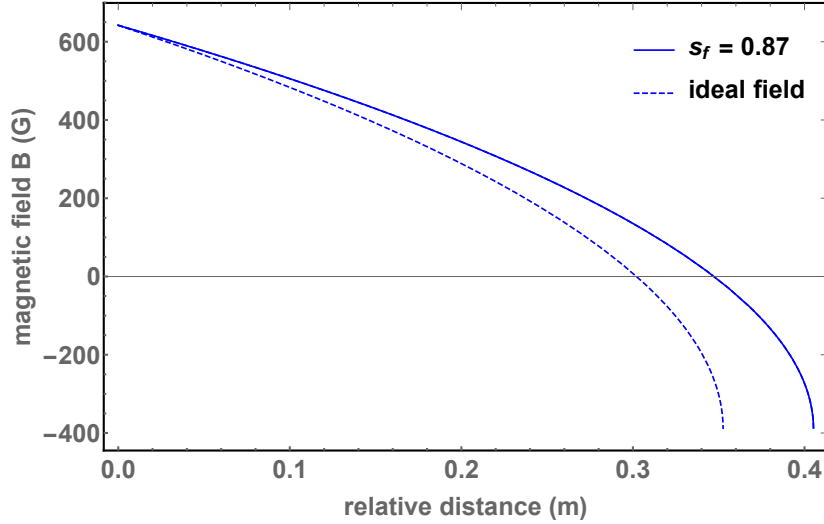


Figure 5-1: Theoretical field for the Dysprosium Zeeman slower. Atoms are slowed down for a starting velocity lower than 645 m/s to a end velocity of 8 m/s. The field was calculated for the ideal case (blue, dashed) and a Zeeman slower with a security factor of 0.85 (blue line)

By choosing the detuning δ three different possible types of a Zeeman slower can be realised.

A Zeeman slower can be realised in three possible types. The first case is the decreasing field Zeeman slower. In this case the atoms at rest are in resonance with the slowing light ($\delta = 0$). During the flight the magnetic field shifts the energy levels to compensate for the Doppler

shift. With lower velocity a decreased magnetic field is needed to slow the atoms further. The advantage of this type is, that the maximum magnetic field is farthest away from the MOT chamber, not disturbing the field inside. Only small stray fields have to be compensated. Due to the small detuning, atoms are heated up when the cooling beam passes through the atom cloud trapped in the MOT.

Another type is the increased magnetic field Zeeman slower. The detuning is chosen to compensate the Doppler shift for the fastest atoms. The magnetic field increases over the length of the Zeeman slower, with the maximum magnetic field at the end. This results in a large residual magnetic field inside the MOT chamber. A strong compensation coil is needed to avoid disturbance of the MOT.

The last and used type for the new Zeeman slower is the spin flip Zeeman slower. The magnetic field at the beginning is lower than for the decreasing field Zeeman slower. The slowing beam is red detuned. At some point, the field changes from a positive field to a negative field. This so called zero-crossing is determined by the detuning δ_0 . The advantage of this type is that overall lower magnetic fields are needed. Lower currents can be used to reach the needed maximum magnetic field, simplifying the construction process. The two different parts can be constructed independently. The difficulty during the construction of the Zeeman slower is to exactly hit the position of the magnetic field zero-crossing. Small spatial deviations can lead to large differences from the intended field and a possible violation of the resonance condition.

Like in the old Zeeman slower, a capture velocity of 645 m/s and a detuning of the cooling light of $\delta = -18\Gamma$ were chosen [30]. All these considerations result in an total magnetic field change B_0 of 1045 G and a bias field B_{bias} of -395 G. For the narrow-line five-beam MOT a final velocity $v_f = 8$ m/s is needed. The length of the Zeeman slower is then calculated to 40.5 cm.

5.2 Simulation of the magnetic field

To match the theory to a magnetic field produced by a wire-wound Zeeman slower, simulations were performed. To get a fitting magnetic field, each winding was treated as a single loop. The magnetic field of a

single coil with radius R , current I and its axis pointing in direction of the z-axis produces the following magnetic field, with μ_0 as the vacuum permeability:

$$B(z) = \frac{I\mu_0}{2} \frac{R^2}{(R^2 + z^2)^{\frac{3}{2}}} \quad (5.9)$$

For the simulations two different wires were used, a 4 mm x 4 mm wire and a 2 mm x 1 mm wire. The square wire has a hollow core profile, which allows an internal water cooling. The Zeeman slower was wound on a tube with a radius of 14 mm.

The simulated Zeeman slower is separated in three different parts with different currents. Using different current regions has the advantage, that even after the construction small adjustments to the magnetic field can be done by individually optimising the currents. The maximum current applied to the square wire was set to 20 A, as the internal water cooling can be used to prevent excessive overheating. For the small rectangular wire a maximum current of around 10 to 12 A was chosen to prevent damage to the insulator material.

The bulk of the Zeeman slower was simulated with the square wire, the rectangular wire was used for field corrections and to generate the high negative magnetic field. To achieve this high field a lot of layers are needed. Using the rectangular wire allows a large number of layers in this part without blocking the optical access to the MOT chamber. At first a standard round wire was chosen with 1 mm diameter for this part. But switching to the rectangular wire allows higher currents to be applied due to the large area, as well as an easier positioning during the construction.

The magnetic field of the Zeeman slower is then the superposition of the magnetic fields produced by the single windings. This simulated field is shown in figure 5-2. By varying the number of layers for each winding, changes to the magnetic field can be easily done.

The difference between the simulated magnetic field and the ideal field for a security factor of 0.85 is shown in figure 5-3. For most of the length of the Zeeman slower the deviations are less than ± 2 G. The only strong divergence are at the end and the beginning of the Zeeman slower, where the field has to reach the desired values. To control,

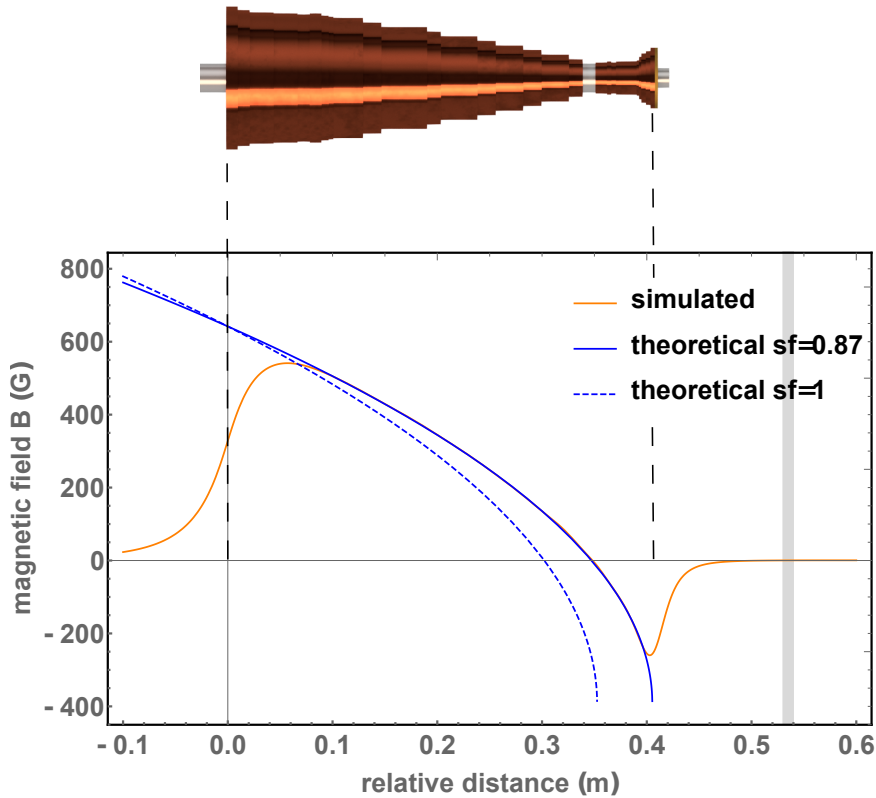


Figure 5-2: **Top:** CAD model of the simulated Zeeman slower. **Bottom:** Corresponding simulated magnetic field for the Zeeman slower (orange). It consists of three different parts. The first part is operated with 17.4 A, the second with 5.7 A and the last part with -10.3 A. In blue are the theoretical fields for the ideal case (dashed) and the adjusted field (line) included. The grey area marks the position of the MOT.

if adiabatic cooling and the resonance condition are fulfilled over the whole length of the Zeeman slower, the slope of the ideal and simulated magnetic field was calculate, see figure 5-4. A violation would lead to the loss of atoms, as the atoms can no longer be cooled and continue with their current velocity. As no crossing of the two lines occurs, the conditions are met and no atoms are lost in the cooling process.

For the current flowing in the square wire, the simulations resulted in a current of 17.1 A. The negative magnetic field will be produced by a current of -10.3 A, the magnetic field corrections with the rectangular

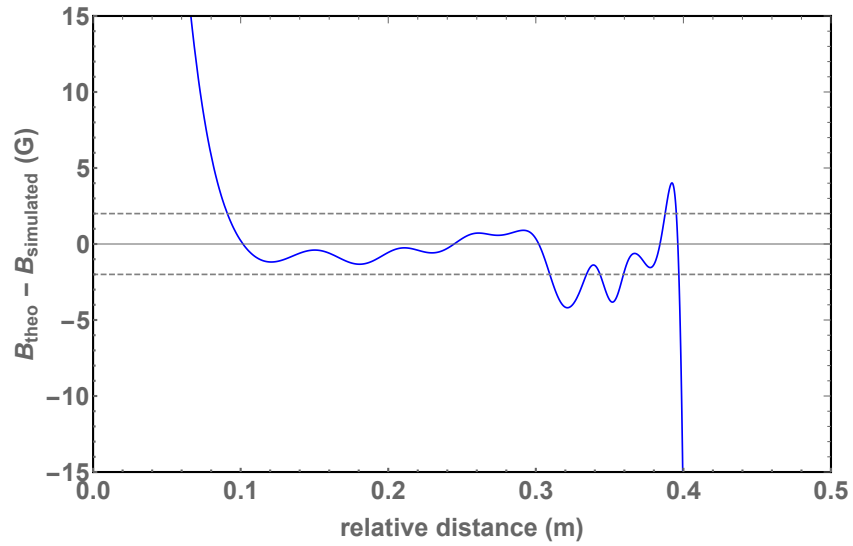


Figure 5-3: Difference between the theoretical and simulated field. For most of the time the deviations are under 2G indicated by the horizontal lines.

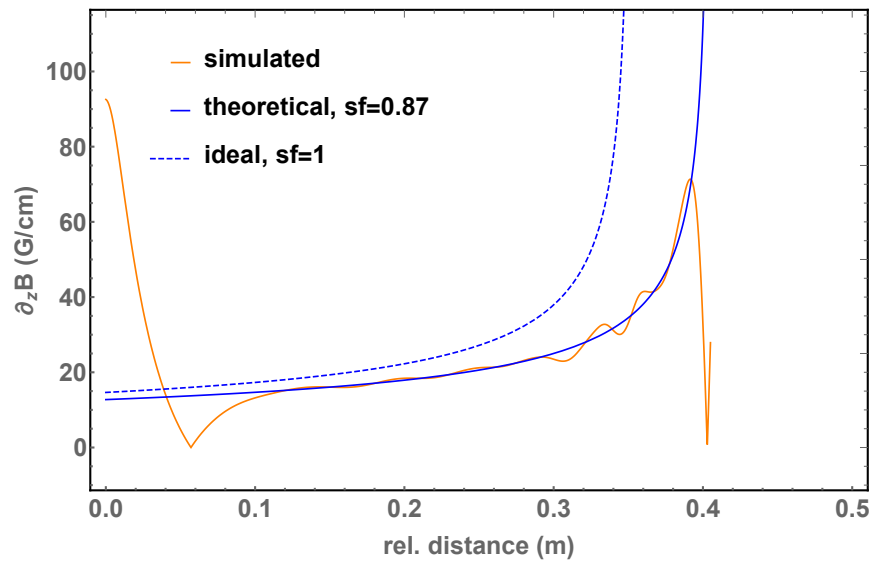


Figure 5-4: Slope of the magnetic field (orange). The slope does not cross the line for the ideal case (blue, dashed). So the resonance condition is valid for the whole length of the ZS and no atoms can leave the deceleration process.

wire on top of the bulk part with 5.5 A. A schematic of the winding plan corresponding to the simulated magnetic field is shown in figure 5-5

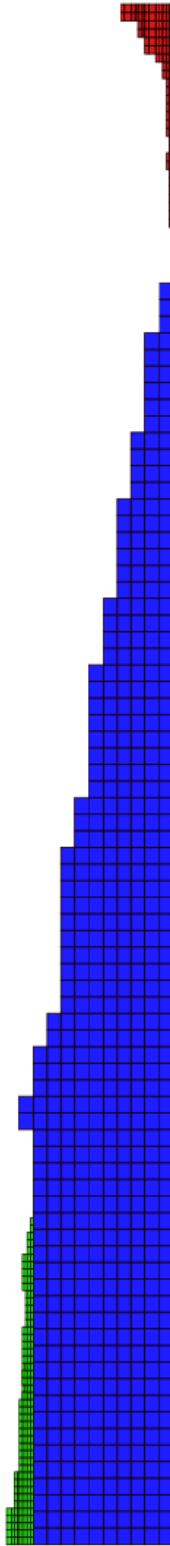


Figure 5-5: Winding plan to produce the simulated magnetic field. The blue part consists of a hollow core wire with 17.1 A. The current for the rectangular wire is 5.5 A in the green part and -10.3 A in the red part, producing there the negative field.

5.3 Atomic flight trajectories calculations

To control, if the simulated field satisfies the requirements, atomic trajectories along the z-axis were simulated. The equation of motion for different starting velocities v_0 were solved numerically and the end velocity at the position of the MOT was obtained [36].

For the simulation, discrete time intervals Δt were chosen

$$\Delta t = \frac{v_0/a_{max}}{N}, \quad (5.10)$$

where N is the number of time steps, varied between 1200 and 20000, depending on the initial longitudinal velocity of the atom

$$B(z) = B_{bias} - B_0 \sqrt{1 - \frac{2a(\delta(z))z}{v_0^2}} \quad (5.11)$$

with

$$\delta(z) = \omega - \omega_0 + kv(z) + \frac{\mu' B(z)}{\hbar}. \quad (5.12)$$

With $a(\delta(z))$ obtained by equation 5.11 and equation 5.12, the velocity can be calculated for a given starting velocity v_0 and a starting position $z=0$. The flight trajectory is then obtained by applying equation 5.13 and equation 5.14 iteratively.

$$v_z(t + \Delta t) = v_z(t) - a(\delta(z))\Delta t \quad (5.13)$$

$$z(t + \Delta t) = z(t) + \frac{1}{2}(v_z(t) + v_z(t + \Delta t))\Delta t \quad (5.14)$$

The results of the atomic flight simulation are shown in figure . For velocities higher than 600 m/s no noticeable slowing-down of the atoms is observed. Due to the high negative magnetic field, atoms are still slowed after leaving the Zeeman slower, reaching a longitudinal velocity of around 8 m/s at the position of MOT (grey area). Not every atom captured by the Zeeman slower can also be trapped by the MOT as they never reach the capture region. For starting velocities lower than 150 m/s, the atoms are slowed down too fast and do not reach the MOT region.

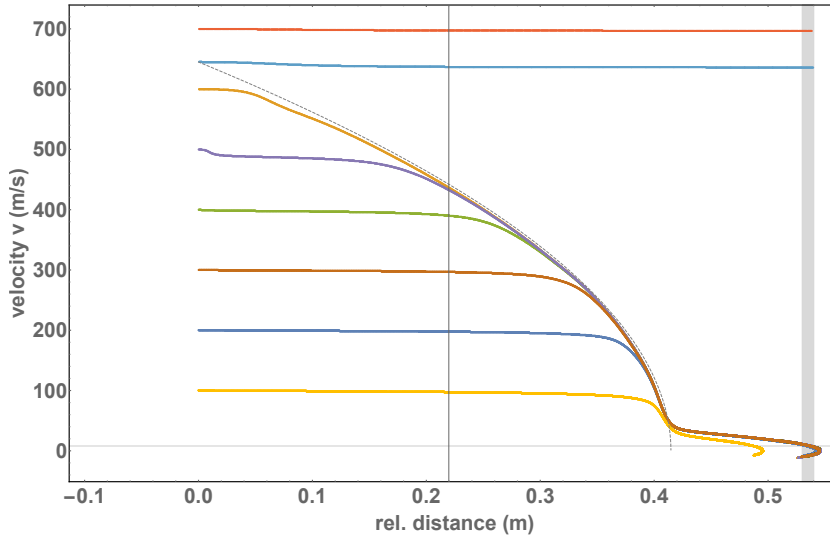


Figure 5-6: Simulation of the atomic flight trajectories inside the ZS. The capture velocity is around 600 m/s, velocities lower than 150 m/s are slowed down too fast. The end velocity in the MOT region (grey area) is 8 m/s.

5.4 Construction of the Zeeman slower

Before the Zeeman slower could be wound, several technical questions first had to be clarified. Heating due to high currents could damage the wire insulator. A decision was made against mounting the Zeeman slower directly on the MOT chamber, as it would fix the position of the Zeeman slower permanently. Instead, the Zeeman slower was wound onto a 316Ti stainless steel tube with a outer diameter of 28 mm and a wall thickness of 2 mm. The tube is not directly mounted to the MOT chamber. Instead a CF16 tube works as a vacuum tube, while the Zeeman slower tube acts as an overtube. This method not only allows to re-position the Zeeman slower after generating the vacuum without opening the setup, but also reduces possible strain on the tube flange since the Zeeman slower has a non negligible weight. Due to the mounting technique, on the side pointing in the direction of the 2D cooling section no flange can be directly attached to the tube. To solve this problem, only a knife edge is attached to the end of this tube. With a homemade splitting [37] the CF16 tube can then be mounted on the cooling section. A schematic drawing of the mounting setup is shown in figure 5-7.

Due to the large current of 10 A in the last part of the Zeeman slower, this part is externally water-cooled. Removing the heat is necessary to

prevent damage of the wire insulation. Water-cooling is done by a 3 mm thick copper disk and an internally water-cooled copper block with an inverted wire profile.

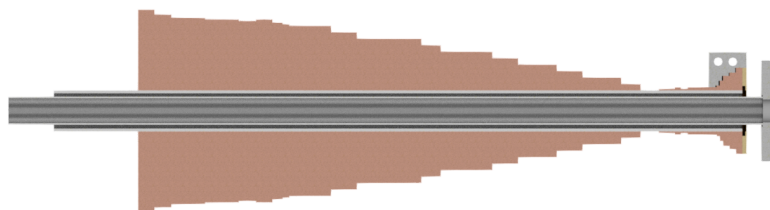


Figure 5-7: Schematic drawing of the mounting of the Zeeman slower. A CF16 tube is used as vacuum tube, the Zeeman slower is wound directly on a overtube with larger diameter.

As a result of using an overtube, the screws for flange connecting the vacuum tube to the MOT chamber can be easily accessed and the Zeeman slower can be positioned as close as possible near the chamber to reduce spread of the atomic beam. A rotatable CF16 flange cut in half can then be placed around the knife edge. By pressing it together and against a copper gasket, the splitting can be connected to the opposite flange at the gate valve.

For winding the Zeeman slower two different wires were used. The bulk is done with a hollow core square $4 \times 4 \text{ mm}^2$ copper wire. The hollow core has a 2.5 mm diameter, resulting in an included water-cooling. It carries a current of 17.4 A. The wire is insulated with a kapton insulation¹, to prevent short-circuits between the different layers. The second wire used is a $1 \times 2 \text{ mm}^2$ rectangular magnetic wire. In the part producing a negative magnetic field it carries a current of -10.3 A, in the part on top of the hollow core wire a current of 5.7 A. Between every layer a separate layer of kapton insulation band² was wound around the tube or the previous layer as safety precaution. For small radii damage to the insulation could occur, so during the winding process the wire was permanently checked for damages. To fix the positions of the individual windings, a two component glue³ with a processing time of six minutes was used. During the winding process, the Zeeman slower was regularly

¹This increases the wire edge length to 4.3 mm.

²Tesa kapton masking tape 51408

³Araldite 2012

checked for short circuits between the layers and their respect to the tube. The magnetic field was measured with a Hall sensor⁴ mounted on a wooden stick for the low magnetic permeability and compared to the simulated magnetic field of the corresponding layer.

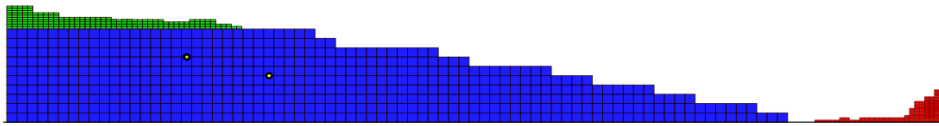


Figure 5-8: Revised version of the winding plan for the Zeeman slower. Changes in effective wire edge length resulted in small changes in the hollow core wire (blue) and the top part (green). The negative part (red) was completely redesigned. The yellow dots mark the position of temperature sensors.

	simulated values	adjusted values
current bulk part I_1	17.1 A	17.4 A
current top part I_2	5.5 A	5.7 A
current negative field I_3	-10.3 A	-10.3 A
edge length hollow core wire	4.3 x 4.3 mm	4.4 x 4.4 mm
edge length rectangular wire	2 x 1 mm	2.2 x 1.1 mm
Zeeman slower length	41.1 cm	42.1 cm
security factor	0.87	0.85

Table 5.1: Adjustment of the winding parameters during the winding process. Imperfections while winding the Zeeman slower result in a deviation of the spacing between two rows. Adapting the edge length leads to changes in several other values.

During the winding process, it was discovered, that a seamless transition between two layers is not possible. This results in several small imperfections, increasing the length of the solenoid. The average wire edge length for the hollow core wire changed to 4.4 mm, and for the rectangular wire to 1.1 (2.2) mm respectively. To account for these changes, a revised version (see figure 5-8) of the winding plan was done during the winding process. This revised winding plan was always developed based on the measured magnetic field of the previous layers. By doing so we were able to continuously correct for deviations from the simulated magnetic field as soon as possible. For the hollow core

⁴Honeywell SS496 A1

wire and the top part only small changes had to be done. A total resimulation of the last part generating the negative magnetic field was performed to calculate the length of the gap between the separate parts of the Zeeman slower. To measure the temperature inside the Zeeman slower two temperature sensors⁵ were included. The size of the sensors caused slight height deviations for the following layers.

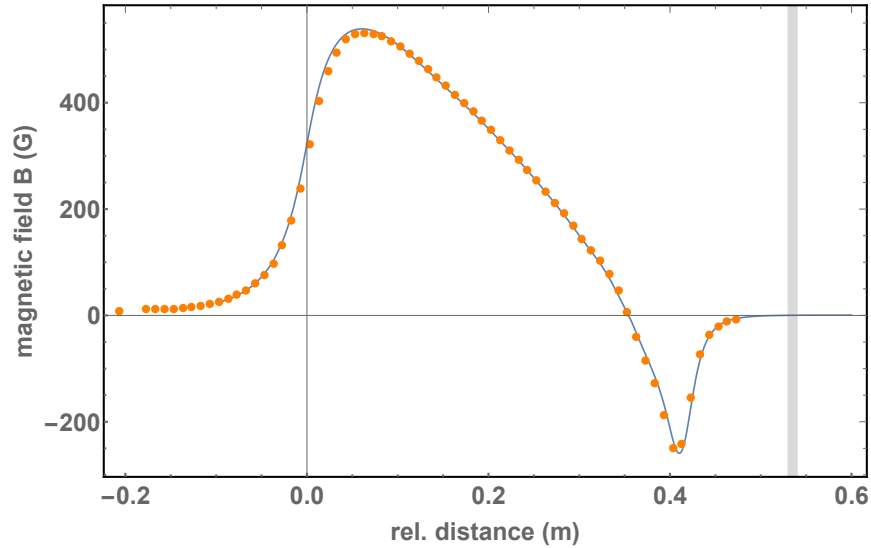


Figure 5-9: Magnetic field measured for fully wound Zeeman slower. The measurement is done with for lower currents due to the limited maximum current of the power supplies. A small deviation for the negative peak can be observed. The grey area marks the position of the MOT.

The measurements for the fully wound Zeeman slower are shown in figure 5-9, 5-10 and 5-11. The measured values are in good agreement with the simulated magnetic field. Only for the negative peak small deviations can be seen. Calculations show, that the windings for the negative part are 2 mm closer to the bulk than intended, resulting in a difference from the calculated magnetic field of up to 20 G. For the most of the length the difference is under 5 G. To look at the influence of the peak shift on the slowing properties of the Zeeman slower, atomic flight simulations for the obtained magnetic field were done. Because of the broad linewidth of the cooling transition, the slowing behaviour is nearly unchanged. Increasing the saturation parameter slightly results again in an velocity at the MOT of around 8 m/s.

⁵Epcos NTC thermistor B57861, 10 k Ω

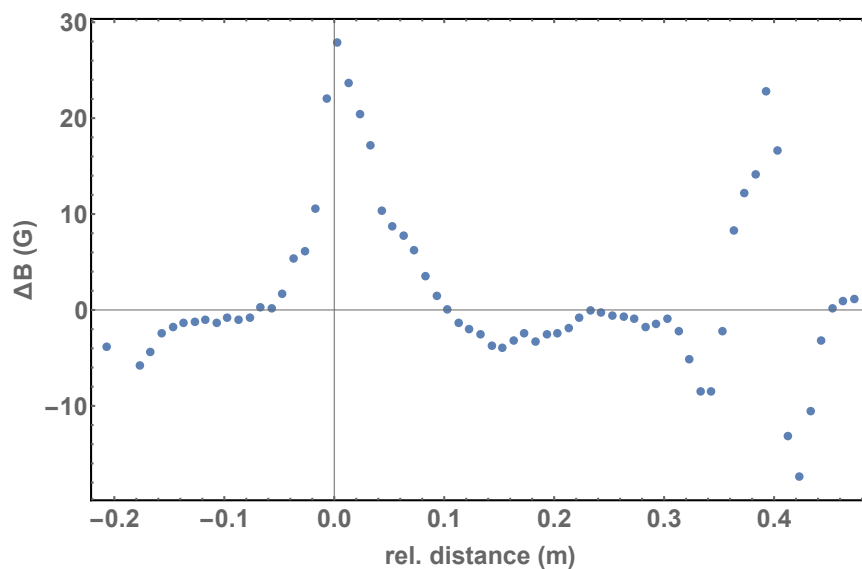


Figure 5-10: Difference between the simulated magnetic field and the magnetic field measured with a Hall probe.

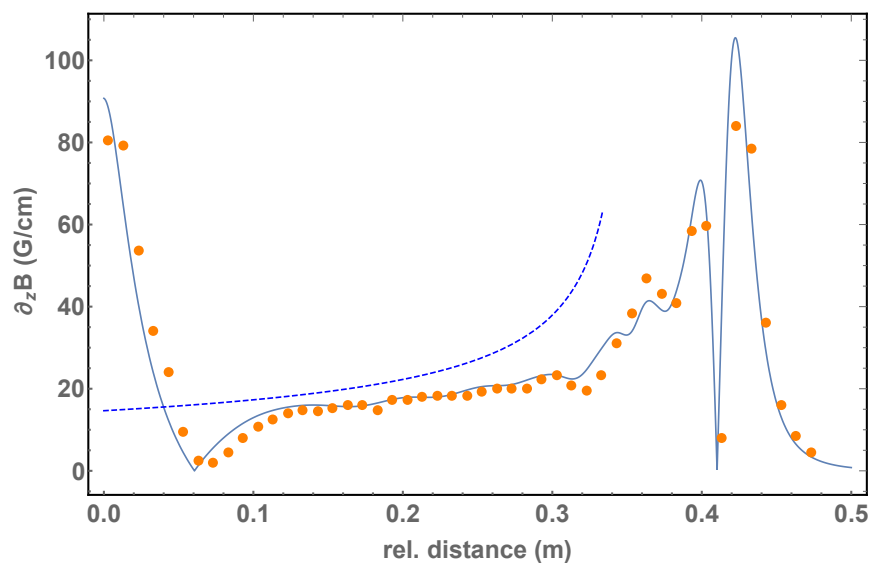


Figure 5-11: Slope of the measured magnetic field. Over the length of the Zeeman slower the slope is lower than the ideal case (blue, dashed), so the resonance condition is fulfilled.



Figure 5-12: Finished Zeeman slower clamped in the lathe. The three different parts are well distinguishable.

Chapter 6

Atom flux

After passing through the Zeeman slower, the atoms are captured in a magneto-optical trap (MOT). For a large number and a fast loading rate, a high atomic flux is needed. In this chapter the divergence behaviour of an atomic beam during the flight through the experimental setup is calculated, as well as the atomic flux reaching the MOT region.

6.1 Beam divergence

After leaving the oven, the atomic beam diverges, while the atoms travel towards the MOT chamber. It is important to investigate the divergence behaviour of the atomic beam, because if the spread is too large, atoms will hit the walls of the vacuum setup and are lost for further experimental use. The spread also influences the number of atoms, which can be trapped inside the MOT. Divergence is caused by several factors [38].

The first influence σ_{nat} is the natural beam broadening caused by the azimuth angle θ under which the atoms leave the oven with an aperture φ_{oven}

$$\sigma_{nat} = \frac{1}{2\sqrt{2}}(\varphi_{oven} + 2\theta(d_{oven} + L)), \quad (6.1)$$

where L is the length of the Zeeman slower and d_{oven} the distance between the oven and the Zeeman slower. Further cause for beam broadening is a transverse diffusion of the atoms, induced by spontaneous emission

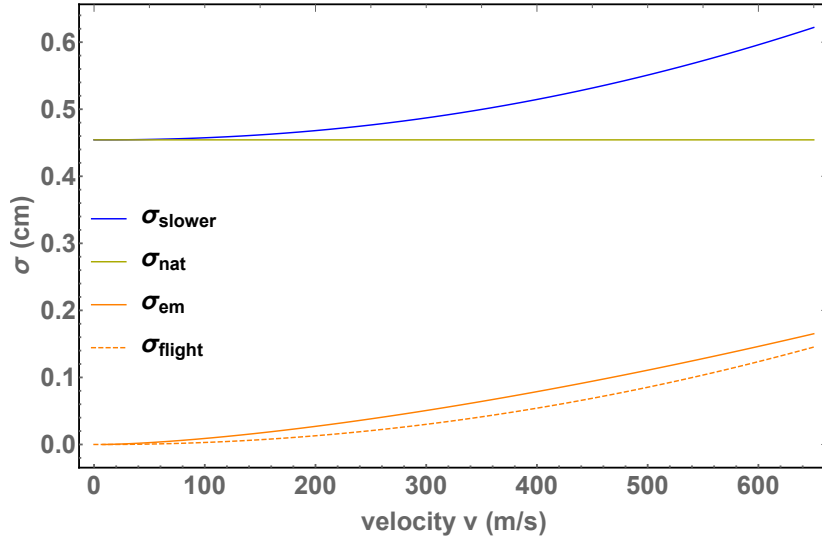


Figure 6-1: Beam broadening (blue) at the end of the ZS depending on the starting velocity. The broadening is caused by several contributions, namely the angle of azimuth at the oven (green), the transverse diffusion due to emission (orange) and the extension of the flight time (orange dashed).

$$\sigma_{em} = \frac{2}{3a_{eff}} \sqrt{\frac{\hbar k}{m}} (v_i - v_f)^{\frac{3}{2}}. \quad (6.2)$$

Here v_i is the initial velocity of the atoms, v_f the velocity after passing through the Zeeman slower and a_{eff} the effective deceleration of the Zeeman slower.

While flying through the Zeeman slower, only the longitudinal velocity of the atoms is slowed down. The transverse velocity remains unchanged. The lower velocity results in an extension of the time of flight and a further beam broadening

$$\sigma_{flight} = \frac{\theta}{2\sqrt{2}} \left(\frac{(v_i - v_f)^2}{a_{eff}} \right). \quad (6.3)$$

The size of the broadened beam at the end of the Zeeman slower can then be calculated by the following way:

$$\sigma_{slower} = \sqrt{(\sigma_{nat} + \sigma_{flight})^2 + \sigma_{em}^2}. \quad (6.4)$$

The impact of these different factors depends strongly on the velocity, with which the atoms leave the oven, as shown in figure 6-1. The strongest influence is the divergence σ_{nat} caused by the angle under which the atoms leave the oven. To minimize this effect transversal cooling is applied in the 2D cooling section.

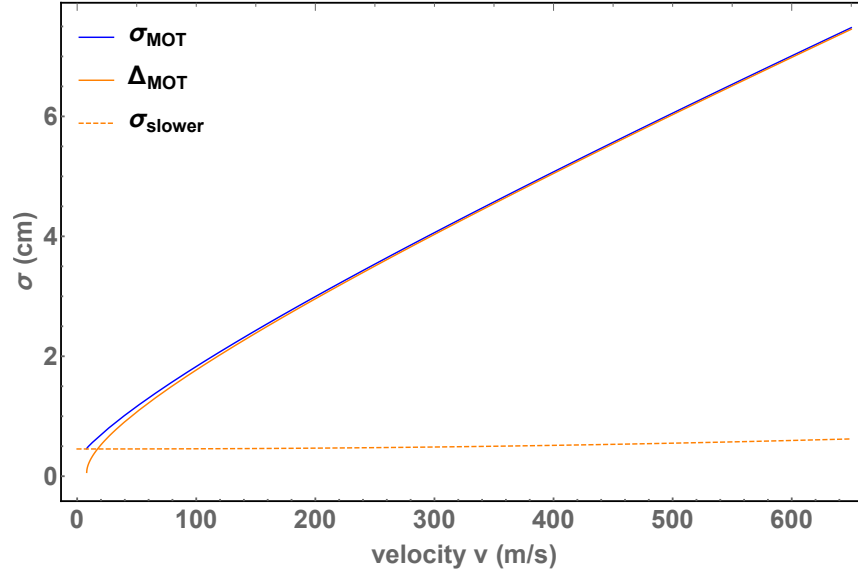


Figure 6-2: Beam broadening at the position of the MOT caused by expansion after leaving the ZS (blue line). The total broadening consists of the broadening caused by the ZS (orange dashed line) and the beam expansion (orange line). The position of the MOT causes the strongest effect.

As mentioned before, the size of the broadend atomic beam is influencing the capture behaviour of the MOT. The broadening σ_{MOT} in the MOT plane is caused by two factor: The spread while travelling through the Zeeman slower σ_{slower} and the spread after leaving the Zeeman slower Δ_{MOT}

$$\sigma_{MOT} = \sqrt{\sigma_{slower}^2 + \Delta_{MOT}^2}. \quad (6.5)$$

Due to drastically reduced longitudinal, but unchanged transversal velocity of the atoms at the end of the Zeeman slower, a strong divergence of the atomic beam happens inside the MOT chamber

$$\Delta_{MOT} = \left(\theta v_i + \sqrt{\frac{\hbar k (v_i - v_f)}{m}} \right) \frac{d_{MOT}}{v_f}, \quad (6.6)$$

where d_{MOT} is the distance of the MOT from the end of the Zeeman slower, v_i the initial velocity, v_f the velocity after leaving the ZS and θ the azimuth angle.

The spread of the atomic beam at the MOT plane depending on the initial velocity of the atoms is shown in figure 6-2. The broadening caused by travelling through the Zeeman slower is low due to the large longitudinal velocity for most of the distance. The influence of the divergence after leaving the Zeeman slower is a lot stronger. The further the MOT is placed away from the end of the Zeeman slower, the less the number of atoms that can be captured inside the MOT. Positioning the centre of the MOT as close as possible towards the Zeeman slower end is crucial for a high atom number. To increase the number of atoms further, the transversal cooling stage is used to decrease the transversal velocity component of the atomic beam. By collimating the atomic beam before entering the Zeeman slower σ_{nat} can be decreased, resulting in a smaller divergence during the flight.

6.2 Atomic flux calculations

An important factor for designing a cold atom experiment is the behaviour of the atomic beam at the position of the MOT. Loading time and atom number are dependent on the atom flux at this position. To estimate the atomic flux at the MOT position, the total atomic flux Φ_0 emitted by the oven has to be estimated first:

$$\Phi_0 = \sqrt{\frac{2\pi}{mk_B T}} \frac{\varphi_{oven}^2}{8} p(T) \sin^2(\theta) \quad (6.7)$$

The total flux is not only dependent on the properties of the oven, namely the aperture diameter φ_{oven} and the azimuth angle θ , but also on the temperature T and the vapour pressure $p(T)$ of the atoms. The vapour pressure of Dysprosium can be approximated by the Antoine equation [39]

$$p(T) = 10^{a - \frac{b}{c+T}} \quad (6.8)$$

with $p(T)$ the pressure of the gas in mbar and T in $^{\circ}\text{C}$. a, b and c are empirical constants [40], which are different for each chemical element. For the approximation $a = 6.92$, $b = 10169.5$ and $c = 36.94$ were used. The temperature dependent vapour pressure for Dysprosium is shown in figure 6-3. To reach a high atomic flux a high temperature is needed, achieved by the use of an effusion cell in the experiment.

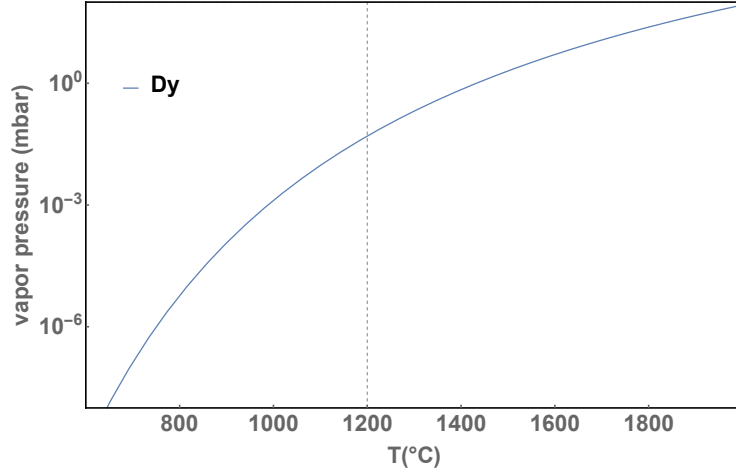


Figure 6-3: Vapour pressure dependent on Temperature for Dysprosium. A high temperature of 1200 $^{\circ}\text{C}$ is required to reach the needed vapour pressure and atomic flux.

The atomic flux at the position of the MOT is reduced by several factors. The first factor η_1 is, that Dysprosium exists in several different isotops. Only atoms of the suitable isotope corresponding to the set laser parameter can be cooled and subsequently captured in the MOT with the 421 nm laser. In the experiment the isotope ^{164}Dy is used, which has a natural abundance of 28.26 %. The other isotops have similar abundances (see chapter 3.1).

Second, only a proportion of the emitted atoms are slowed down by the Zeeman slower. Atoms leaving the oven with a velocity higher than the capture velocity $v_{c,max}$ of the Zeeman slower can not be captured inside the MOT, as well as atoms are slowed down too much $v_{c,min}$ to reach the MOT region (see figure 5-6). The velocity distribution of the atoms follows a modified Boltzmann distribution [37]

$$f(v) = 2 \left(\frac{m}{2k_B T} \right)^2 v^3 e^{-\frac{mv^2}{2k_B T}}. \quad (6.9)$$

Therefore the proportion of slowable atoms η_2 reduces the atomic flux further

$$\eta_2 = \frac{\int_{v_{c,min}}^{v_{c,max}} f(v)dv}{\int_0^\infty f(v)dv}. \quad (6.10)$$

The last factor η_3 is, that the atomic beam is broadend after leaving the Zeeman slower as discussef in the previous section. Not every atom, which is slowed and reaches the MOT region, passes through the capture range of the MOT.

$$\eta_3 = \frac{\text{atoms inside capture range}}{\text{total slowed atoms}} \quad (6.11)$$

The intensity profile of the atomic beam at the MOT position is calculated with an Gaussian ansatz

$$I_i(x) = \frac{1}{\sqrt{2\pi}\sigma_{MOT,i}} e^{-\frac{x^2}{2\sigma_{MOT,i}^2}}, \quad (6.12)$$

where $\sigma_{MOT,i}$ is the calculated beam expansion as in section 6.1 for every initial velocity ($0 < v_i < v_c$). The total beam intensity is then obtained by an integral over the intensity for each velocity, weighted with the modified Boltzmann distribution $f(v)$ (shown in figure 6-4)

$$I(x) = \int_0^{v_{max}} f(v_i)I_i(x)dv_i. \quad (6.13)$$

The captured fraction of atoms inside the MOT region with a capture radius r_c can then be calculated by

$$\eta_3 = \frac{\int_0^{r_c} I(r)dr}{\int_0^\infty I(r)dr}. \quad (6.14)$$

Each of these three factors leads to a reduction of the total atomic flux, so only a fraction of the atoms Φ_{MOT} can be trapped inside the MOT

$$\Phi_{MOT} = \eta_1 \cdot \eta_2 \cdot \eta_3 \cdot \Phi_0. \quad (6.15)$$

For an oven temperature of 1200 °C and a capture velocity of 645 m/s

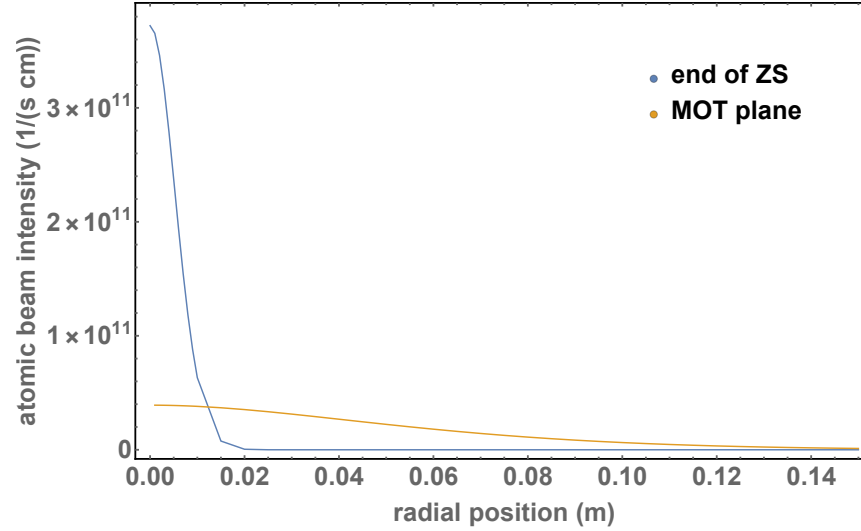


Figure 6-4: Transverse intensity distribution at the end of the Zeeman slower (blue) and at the MOT plane (orange). Due to relative large transverse velocity of the atoms a large radial spread can be observed in the MOT plane.

of the Zeeman slower the total atomic flux produced by the oven is $6.49 \cdot 10^{11}$ atoms per second. Calculating these factors $\eta_1 = 0.2826$, $\eta_2 = 0.7625$ and $\eta_3 = 0.2356$ results in an atomic flux at the MOT position of $3.23 \cdot 10^{10}$ atoms per second, enough for loading for a fast and efficient loading of the MOT.

Chapter 7

Vacuum simulations

In this chapter the pressure behaviour of the vacuum system is analysed. Pumping speed and placement of the vacuum pumps is examined to guarantee that an ultra high vacuum region can be generated inside the experiment chamber. Additionally the influence of an integrated pumping port at the MOT chamber and the design of the transport tube towards the science cell is investigated.

First a short overview over the general concepts of vacuum systems will be given. The pressure inside the vacuum apparatus is strongly determined by its intended purpose. To understand the pressure behaviour inside the vacuum system, the parameters of the gas flow have to be characterised first. The pumping speed S is defined as the flow rate through an aperture or a tube cross section [41]:

$$S = \frac{dV}{dt} \quad (7.1)$$

The conductance C describes the ability of a tube to transmit gas. The pressure difference on both sides and the conductance of a tube determines the throughput Q of the tube

$$Q = C \cdot (P_1 - P_2). \quad (7.2)$$

As the throughput of a vacuum tube is limited by the conductance, not all of the pumping power can be applied. The pumping speed of a vacuum pump is reduced by the design of the vacuum system. The effective pumping speed S at the tube end for a pump with a pumping speed S_p is:

$$S = \left(\frac{1}{S_p} + \frac{1}{C} \right)^{-1} \quad (7.3)$$

According to [41] the conductance C of a tube with length L and a diameter D can be calculated as

$$C = 2.6 \cdot 10^{-4} \bar{v} \frac{D^3}{L} \text{ l s}^{-1} \stackrel{\text{air,20}^\circ}{=} 12 \frac{D^3}{L} \text{ l s}^{-1}, \quad (7.4)$$

where \bar{v} is the mean thermal velocity of the atoms.

Due to the reduction of the pumping speed, the position of the vacuum pumps and their pumping speed is critical for achieving very low pressure inside the system. Tubes with a small diameter result in a low effective pumping speed. To prevent this issue, an important parameter to consider and adjust is the conductance of the individual vacuum parts.

7.1 Simulation model

For a stable lattice with a small wavelength of 362 nm inside the science cell, an ultra-high vacuum ($\sim 10^{-12}$ mbar) inside the MOT chamber and science cell is required. The Zeeman slower acts as a differential pumping stage. With this technique, a large pressure difference between two different sections of a vacuum setup can be maintained. The pressure difference is preserved by a small aperture between the two sections and an additional pumping in the lower pressure section. The requirements on the vacuum inside the 2D cooling section are not so severe ($\sim 10^{-9}$ mbar). No experiments will be done in this section. To investigate the pressure behaviour inside the experimental setup, vacuum simulations were done. The influence of the pump position and the pumping speed was examined, as well as the influence of a running oven. The program used was Molflow⁺¹, which uses a Monte-Carlo algorithm to simulate trajectories of particles in high vacuum conditions to calculate the pressure.

To simplify and speed up the simulation time, a simple CAD model of the inner volume of the experimental setup was made (see figure 7-1). Each surface is assigned an outgassing rate of $3 \cdot 10^{-12} \frac{\text{mbar} \cdot \text{l}}{\text{s} \cdot \text{cm}^2}$ for

¹Version 2.6.70

stainless steel [42, 43]. For fused silica the outgassing rate is hard to determine and therefore was set to the one of stainless steel.

Areas with pumps do not get an outgassing rate assigned, but instead an appropriate pumping speed is applied to them. Finally the outgassing rate and temperature at the surface of the oven is increased to simulate the vacuum behaviour in the case of a running experiment.

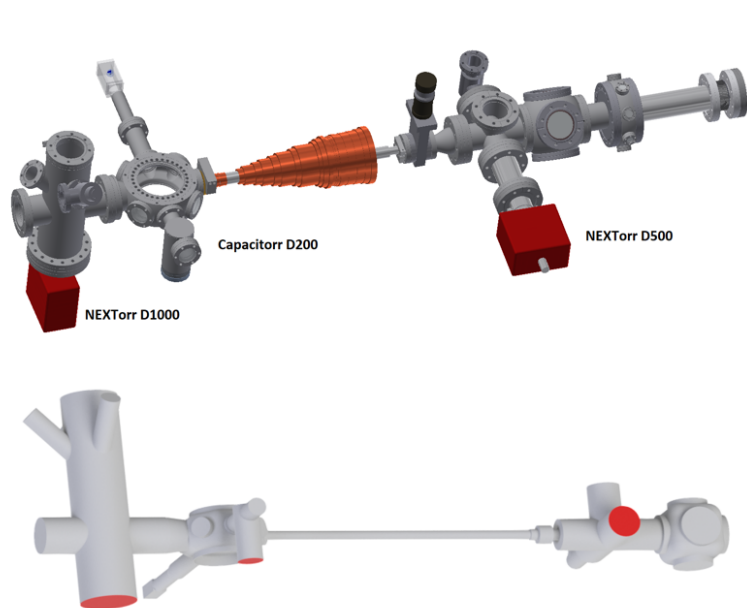


Figure 7-1: **Top:** Simplified drawing of the setup with marked pump positions. **Bottom:** Schematic CAD model of the interior of the vacuum setup used for the vacuum simulations. The positions of the pumps are marked in red.

Near the 2D cooling a NEXTorr D500 Starcell² with a H₂ pumping speed of 500 l/s was placed, directly at the MOT chamber a Capacitorr D200 with a pumping speed of 200 l/s and under the pumping cross a NEXTorr D1000 with 1000 l/s. All simulations were done for a residual gas of H₂ atoms. The simulation program can only run simulations for one type of gas inside the vacuum setup. Hydrogen is the main gas to take care of in UHV sections.

The small D200 getter pump was in later simulations substituted to a pump Z200 with a new alloy, changing the pumping speed to 290 l/s.

²All vacuum pumps are manufactured by SAES.

7.2 Integrated pumping port

Due to geometric constraints, not the full pumping speed of all the vacuum pumps can be effectively applied. Connecting passages with a small diameter or long passages have a low conductance and limit the effective pumping speed, which can be applied [41]. To increase the conductance between the pumping cross and MOT chamber, one port of the octagon was modified. Instead of a normal port a integrated pumping port with larger cross section was include. According to the manufacturer of the MOT chamber³, the integrated pumping port increases the conductance from 53 l/s to 180 l/s.

To analyse the influence of the conductance increase, simulations for the modified MOT chamber and a standard octagon with a conical reducer at one port were performed (figure 7-2). Both simulations were done for one vacuum pump (NEXTorr D1000) with a pumping speed of 1000 l/s placed at the same position.

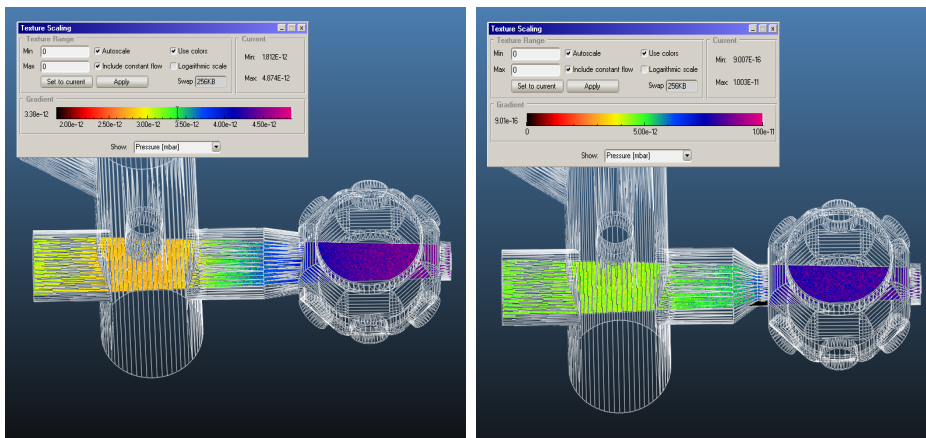


Figure 7-2: Comparison of the pressure behaviour between the modified MOT chamber (left) and a standard octagon with added conical reducer. The pressure inside the standard chamber is $1 \cdot 10^{-12}$ mbar higher than for the modified version.

The effect of the increased conductance of the intergrated pumping port is shown in figure 7-3. For the modified version the pressure decreases from $3.6 \cdot 10^{-12}$ mbar to $2.7 \cdot 10^{-12}$ mbar in comparison to the standard version.

For the standard octagon a sudden rise in pressure at the position of the reducer can be observed. Due to the lower conductance of the small port, the effective pumping speed is reduced greatly. In the modified

³Kimball Physics, spherical octagon with integrated pumping port

version with integrated pumping port, more particles from the MOT chamber can be pumped, resulting in an overall lower pressure and a very small increase in pressure between the pumping cross and the MOT chamber.

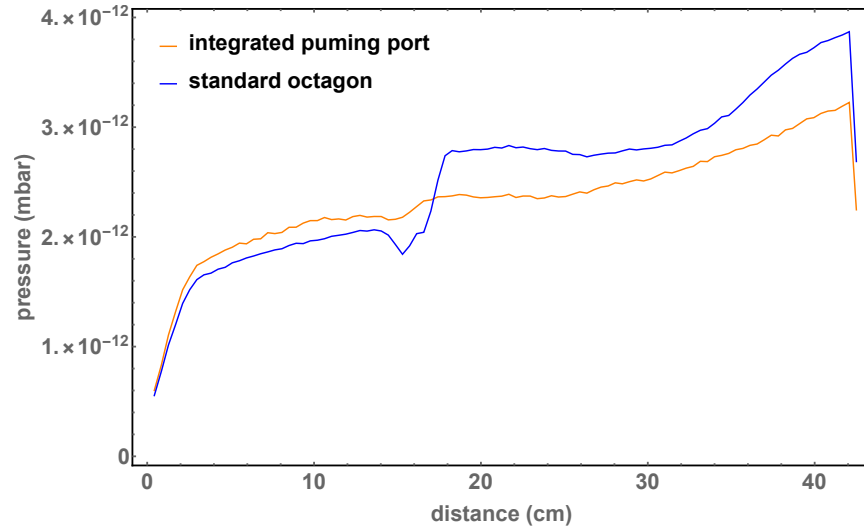


Figure 7-3: **Top:** Pressure simulation for the integrated pumping port. The red line marks the axis along which the pressure was simulated. **Bottom:** Pressure profile for the modified version (orange) and the standard version (blue). The MOT chamber is located on the right side. At the connection between the standard MOT chamber and reducer, a jump in pressure is observed. For the integrated pumping port a overall lower pressure inside the MOT chamber can be seen.

7.3 Transport tube to science cell

Another important aspect for understanding the pressure behaviour of the setup is the influence of the transport tube diameter, connecting the MOT chamber and the science cell. As most of the experiments will be done inside the science cell, a very high vacuum is needed inside the glass cell. A small diameter and long length of the transport tube drastically decrease the conductance and effective pumping speed. While a short connection to the science cell would be feasible, the length of the transport tube is fixed by the space needed for the necessary magnetic shielding. This constraint will heavily limit the effective pumping speed inside the science cell.

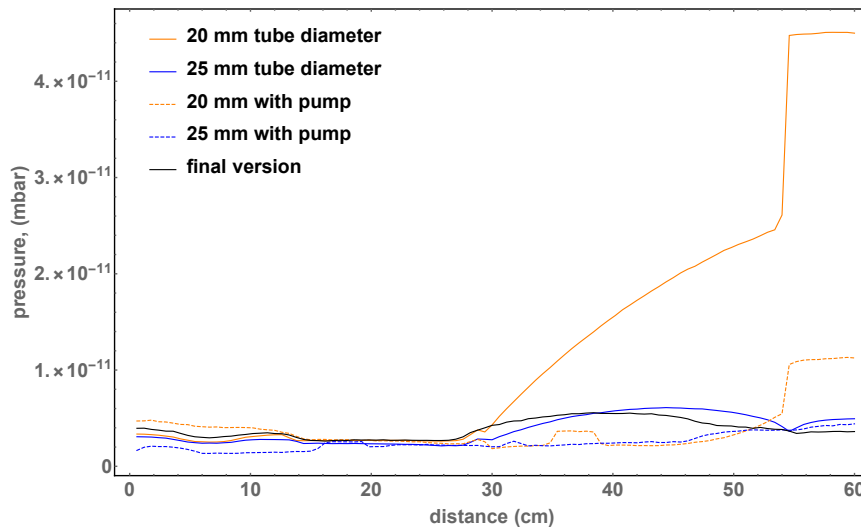


Figure 7-4: **Top:** Pressure simulation for different transport tube diameters. The red line marks the axis along which the pressure was simulated. **Bottom:** Increasing the diameter from 20 mm to 25 mm reduces the pressure by a factor of 10. Additional reduction can be achieved by placing the getter pump between MOT chamber and science cell.

For the tube diameter, two different diameters (20 mm and 25 mm) were chosen to analyse the effect in the pressure inside the science cell. Additionally the option of moving the ion getter pump between the MOT chamber and science cell was simulated, as well as a transport tube with changing tube diameter.

Simulations were done for a tube length of 250 mm and tube diameters of 20 mm and 25 mm and an inner volume of the science cell of

$(35 \cdot 25 \cdot 60) \text{ mm}^3$. With the help of equations 7.4 and 7.3, a conductance of 3.84 l/s and 7.5 l/s can be calculated. Due to the small diameter the pumping speed of a pump with $S_p = 290 \text{ l/s}$ is reduced to 3.79 l/s and 7.31 l/s respectively. The diameter dependence of the pressure is shown in figure 7-4. As it can be seen, the tube diameter has a strong influence on the pressure behaviour. For a small diameter the conductance is too low to pump the atoms out of the science cell, resulting in a pressure of $4.5 \cdot 10^{-11} \text{ mbar}$. Increasing the tube diameter to 25 mm already decreases the pressure down to $4.7 \cdot 10^{-12} \text{ mbar}$ (figure 7-4).

Moving the getter pump to a position between MOT chamber and science cell can be used to further decrease the pressure. For a tube diameter of 20 mm this effect is stronger, because the pump effects the particles inside the transport tube. As seen before the low conductance prevents a pumping of the particles out of the science cell into the transport tube. Adding the pump decreases the pressure value down to $1.1 \cdot 10^{-12} \text{ mbar}$ for 20 mm diameter and $4.1 \cdot 10^{-12} \text{ mbar}$ for 25 mm diameter. Even without the pump in between, low enough pressure in the region of 10^{-12} mbar can be reached. Therefore the option of a pump between MOT chamber and science cell was dropped for the advantage of reducing potential magnetic stray fields. Additionally, more space for the magnetic shielding is available.

Furthermore an additional version of the transport tube was simulated with a changing diameter. As the tube diameter has a strong influence on the effective pumping speed, a inside diameter of 35 mm was chosen to use the maximum available conductance. After a distance of 162 mm, the tube diameter is reduced to 28 mm. Due to changes in the design of the glass cell, the tube length was changed to 262 mm and the inside volume of the science cell to $(57 \cdot 26 \cdot 24) \text{ m}^3$. This reduces the inside volume to 56 % of the former volume. The conductance for each part of the transport tube can be calculated separately. The total conductance is approximately

$$C = \left(\frac{1}{C_1} + \frac{1}{C_2} \right)^{-1} = 14.4 \text{ l s}^{-1}, \quad (7.5)$$

resulting in an effective pumping speed of 13.7 L/s. Possibilities to increase the pumping speed further are limited by the geometry of the setup. The pressure inside the science cell obtained by the simulations is $4 \cdot 10^{-12} \text{ mbar}$, which is even lower than for the pump added in be-

tween. The effective pumping speed of the tube inside the transport tube is so reduced, that it has only an insignificant impact to the total pumping speed.

Changing the tube diameter and the pump position does not have a strong influence on the pressure inside the MOT chamber. The simulations give a value of around $2.5 \cdot 10^{-12}$ mbar for the standard tubes. For the tube with changing diameters the pressure increases slightly to $3 \cdot 10^{-12}$ mbar.

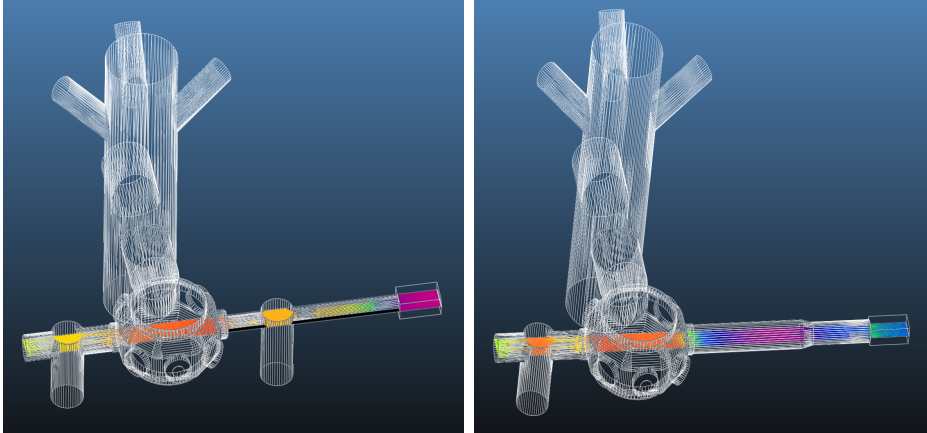


Figure 7-5: Simulation setup for the pressure inside the transport tube to the science cell. **Left:** Simulation for a 20 mm tube diameter with the getter pump added between the science cell and MOT chamber. An additional pump is placed in the transport tube to increase the pumping speed in the science cell. **Right:** Simulation for a tube with changing diameter from 35 mm to 28 mm.

For the lattice inside the science cell a stable pressure and temperature is needed. While pressure fluctuations cannot be simulated with Molflow+, the pressure behaviour over the length of the science cell can be investigated (see figure 7-6). On the side with the transport tube opening, the pressure is much higher ($1.1 \cdot 10^{-12}$ mbar) than in the middle of the science cell ($4.3 \cdot 10^{-13}$ mbar). Hydrogen atoms pumped from the science cell into the transport tube block the way for the following atoms, due to the smaller diameter of the transport tube.

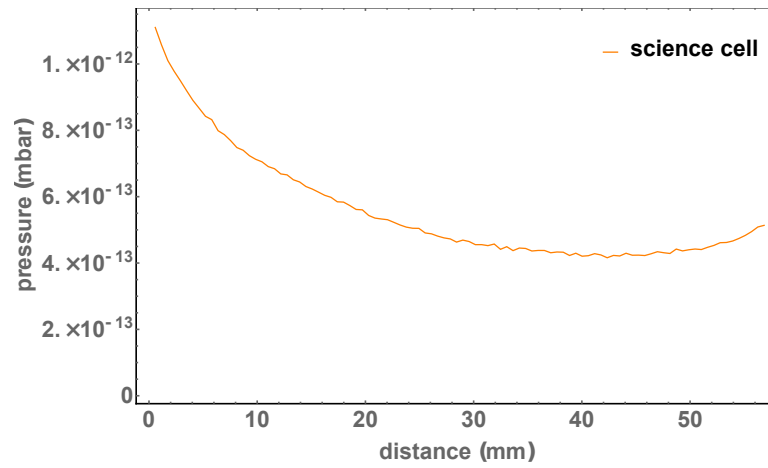
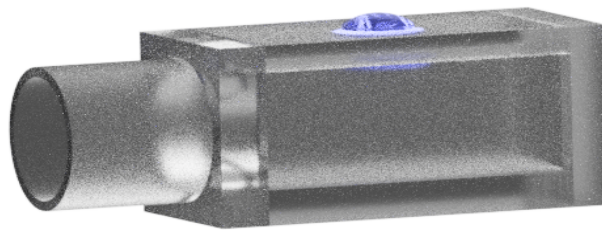


Figure 7-6: Pressure behaviour inside the science cell. The connection to the transport tube is on the left side. The red line marks the simulation axis.

7.4 Influence of the oven

To include the effect of a running oven and the long Zeeman slower tube on the pressure behaviour on the whole setup, the previous used simulation model was expanded for the full vacuum setup, as seen in figure 7-7. Again a pumping speed for H₂ of 1000 l/s at the pumping cross and of 290 l/s at the MOT chamber were used. Additionally a third pump was included near the 2D cooling chamber, positioned at the five-way cross. The pump speed for the third pump was set to 500 l/s.

First the influence on the pressure inside the MOT chamber and the science cell was examined (figure 7-8) for the expanded simulation model. With the third pump and the 2D cooling stage added, a pressure value of $3 \cdot 10^{-12}$ mbar was obtained, which is in accordance with the pressure for only simulating the MOT chamber part. The pressure inside the science cell even decreases down to $5 \cdot 10^{-13}$ mbar.

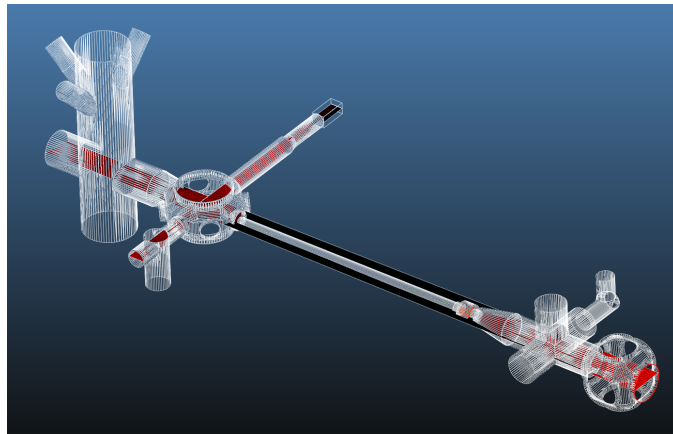


Figure 7-7: Model of the full setup used for simulating the pressure behaviour. The red circle at the oven chamber (right downside corner) marks the position of the oven for simulation purposes.

For simulating a running oven, the temperature at the oven position (red circle in figure 7-7, bottom right corner) was set to 1250 °C and the outgassing rate increased to $3.2 \cdot 10^{-7} \frac{\text{mbar} \cdot \text{l}}{\text{s} \cdot \text{cm}^2}$. A running oven and the thereby emitted Dysprosium atoms to the chamber was mimiced by an increased outgassing rate of the corresponding surface that represents the oven flux.

Adding the increased outgassing rate also increases the pressure both

inside the science cell and the MOT chamber. For the MOT chamber pressure values of $9 \cdot 10^{-11}$ mbar and for the science cell of $1 \cdot 10^{-12}$ mbar are obtained. While the increased amount of particles can travel through the Zeeman slower tube towards the MOT chamber easily and therefore increasing the pressure, the geometry of the MOT chamber hinders a direct movement inside the science cell.

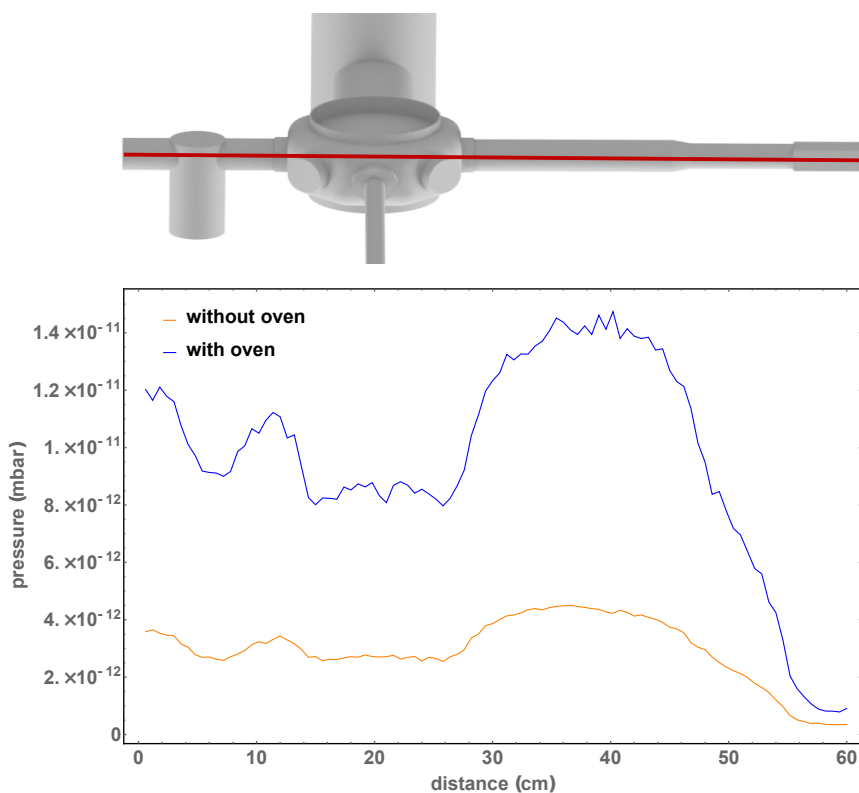


Figure 7-8: Pressure profile for the axis MOT chamber - science cell (left to right) for an increased outgassing rate of $3.2 \cdot 10^{-7} \frac{\text{mbar} \cdot \text{l}}{\text{s} \cdot \text{cm}^2}$ and a temperature of $1250 \text{ }^\circ\text{C}$ at the oven (blue) and without (orange).

Next the influence of the Zeeman slower tube was investigated (figure 7-9). It operates as a differential pumping stage, separating the HV part of the oven section from the UHV part of the MOT chamber. The pressure profile along the axis pumping cross - oven chamber is shown in figure 7-9. For a turned off oven, only a slight increase of the pressure over the experimental setup can be observed. This is caused by the large pumping speed in the pumping cross. Turning on the oven, results in a drastical change inside the 2D cooling chamber. The enhanced temperature and outgassing rate increase the pressure

from $5 \cdot 10^{-12}$ mbar to $4.5 \cdot 10^{-9}$ mbar. The differential pumping effect of the Zeeman slower tube can be clearly observed, separating the two pressure sections.

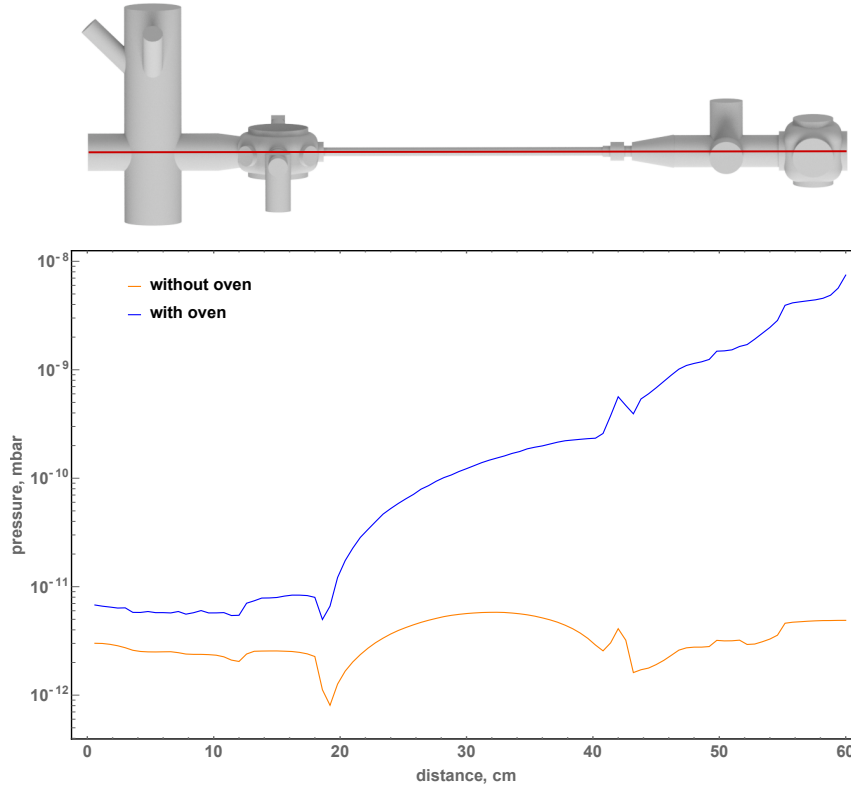


Figure 7-9: Pressure profile for the axis pumping cross - oven (left to right). For a turned on oven an increased outgassing rate of $3.2 \cdot 10^{-7} \frac{\text{mbar l}}{\text{s cm}^2}$ and a temperature of $1250 \text{ }^\circ\text{C}$ were included in the simulation. For a running setup the differential pumping effect of the Zeeman slower can be observed.

The vacuum simulations for the complete setup not only show, that the pumping speed and position of the chosen pumps result in the required vacuum pressure. They also confirm a separating of the HV and UHV section with the Zeeman slower tube as a differential pumping section. Limitations are caused by bottlenecks, which reduce the conductance and the effective pumping speed. To address these issues, a special design of the MOT chamber with an integrated pumping port is chosen. For the transport tube the diameter is kept as large as possible for most of its length. With this, a HV section with $4 \cdot 10^{-9}$ mbar in the 2D cooling chamber and a UHV section with $1 \cdot 10^{-12}$ mbar inside the science cell can be generated.

Chapter 8

Discussion and outlook

This thesis reports on the design of a new quantum gas microscope setup. The main focus is set on a new Zeeman slower and the cooling section. As the experiment will be set up from scratch, several fundamental design decisions had to be settled. Access and path of the laser beams had to be considered, as well as the overall design geometry. Furthermore transport of the atoms through the experiment into the science cell had to be taken into account.

A vacuum apparatus is designed for the creation of a high atomic flux of ultracold Dysprosium atoms. For a fast loading of the magneto-optical trap, a strongly collimated beam is needed. With the help of a transversal cooling stage the atomic beam can be collimated after leaving the oven, increasing the number of atoms inside the magneto-optical trap. The use of CF63 viewports allows the utilisation of large transversal cooling beams. The individual stages of the experimental setup are optimised to ensure a high atomic flux at the position of the magneto-optical trap.

As observed in the current experiment atoms can leave the oven under a large angle of emergence, resulting in a great atom loss for the transversal cooling and a coating of the oven section. With a new design of the crucible and an additional aperture added, a better collimated atomic beam should reach the transversal cooling section. With a higher atomic flux, better operation of the magneto-optical trap is expected.

A central task of this thesis was the construction of a new Zeeman slower. With the new approach of that uses a magneto-optical trap us-

ing only five beams and gravity to capture the atoms, the atoms have to be slowed down to very low velocities. The new Zeeman slower is designed to slow the Dysprosium atoms down from a velocity of around 640 m/s to 8 m/s over a length of 42.5 cm. A spin flip type was chosen, separating the Zeeman slower into two independent parts and reducing the absolute magnetic field strength. Part of the Zeeman slower is internally water-cooled to prevent a potential damage of the wire insulation.

As a second major part of this work, vacuum simulations were performed. To achieve long lifetimes in the optical lattice, a stable ultra-high vacuum in the science cell is necessary. Therefore the ideal arrangement and pumping speed of the vacuum pumps are investigated, to reach the required pressure. The individual parts of the vacuum apparatus are examined in regard to their influence on the effective pumping speed. To guarantee a maximum effective pumping speed in the science cell, the shape of the transport tube between science cell and magneto-optical trap chamber was optimised. With the optimised layout of the vacuum pumps, a pressure of around 10^{-12} mbar in the science cell can be achieved. Inside the transversal cooling section a high vacuum section ($\sim 10^{-9}$ mbar) is sufficient. The long Zeeman slower tube acts as a differential pumping section, separating these two pressure regions.

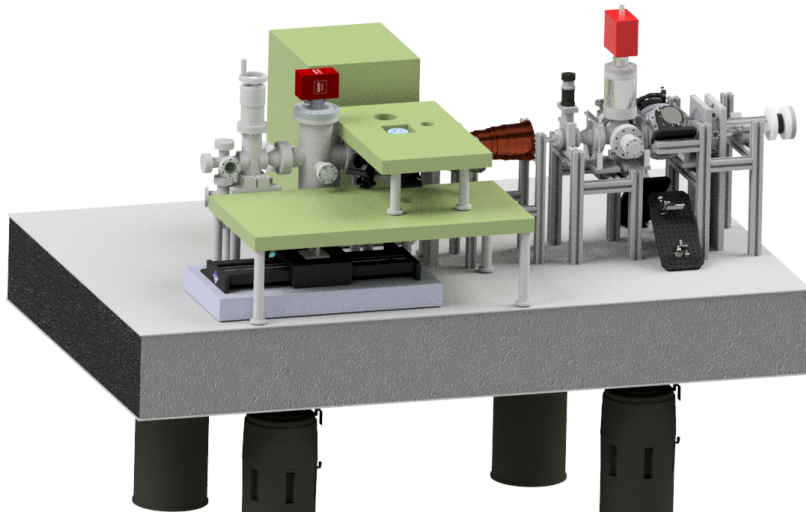


Figure 8-1: Current planning status. Breadboards for the MOT optics and imaging have been added, first design of the magnetic shielding as well.

An overview of the current planning status is shown in figure 8-1. At the moment calculations for the magnetic shielding are performed.

The next step will be setting up the vacuum section of the new experiment. After baking the experimental apparatus at around 150 - 200 °C depending on the involved material and activating the vacuum pumps, the pressure has to be compared to the simulated values, as a ultra high vacuum is needed inside the science cell. Optics and the 421 nm laser have to be set up for the transversal cooling. Afterwards a characterisation of the atomic beam before and after the Zeeman slower via spectroscopy is required. Testing and optimising of the Zeeman slower and setting up the magneto-optical trap is the next step for generating a Bose-Einstein condensate. Finally the lattice and magnetic shielding at the science cell have to be added, before atoms can be transported to the science cell by a optical dipol trap.

Appendix A

Bitter-type coil Zeeman slower

As an alternative design for the Zeeman slower, the concept of using Bitter-type coils [44, 45] to generate the magnetic field was investigated. This idea of a Bitter-type Zeeman slower was proposed by [46].

Bitter-type coils can be used to create high magnetic fields in a compact shape. An additional advantage is, that the coil is already internally water-cooled. Layers of copper and an insulator material alternate and are stacked on each other. The copper rings have a small gap, resulting in a helical current flow through the coil. Current flow through the insulator material is guaranteed by a small copper part. Holes through the whole coil are used for water transport. A design sketch of a typical Bitter-type coil is shown in figure A-1.

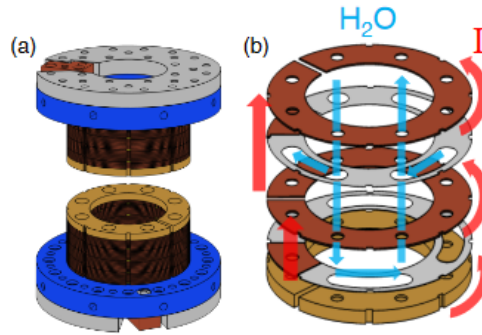


Figure A-1: Schematic drawing of a Bitter-type coil design. The current (red) flows through the coils in a helical pattern. The individual copper layers are separated by insulator material [46].

To simulate the magnetic field for the Zeeman slower, the induced magnetic field for each single copper ring has to be calculated. For the field along the axial direction this can be expressed following [46] as

$$B_z(z) = \frac{\mu_0 d \lambda}{2} \left[j \left(\sqrt{a_1^2 + z^2} \right) - j \left(\sqrt{a_2^2 + z^2} \right) \right]. \quad (\text{A.1})$$

Here a_1 is the inner radius, a_2 the outer radius, d the layer thickness, λ the filling factor of the coil and $j(r)$ the radial current density:

$$j(r) = \frac{I}{d \lambda \ln\left(\frac{a_2}{a_1}\right)} \frac{1}{r} \quad (\text{A.2})$$

The $\frac{1}{r}$ density distribution is a result of the cylindrical symmetry of the coil. The total magnetic field is then calculated by placing the layers with different radii on each other by adjusting their z-position. Due to the large magnetic field difference over the length of the Zeeman slower, it was separated in sections with different currents I . The calculated magnetic field is shown in figure A-2.

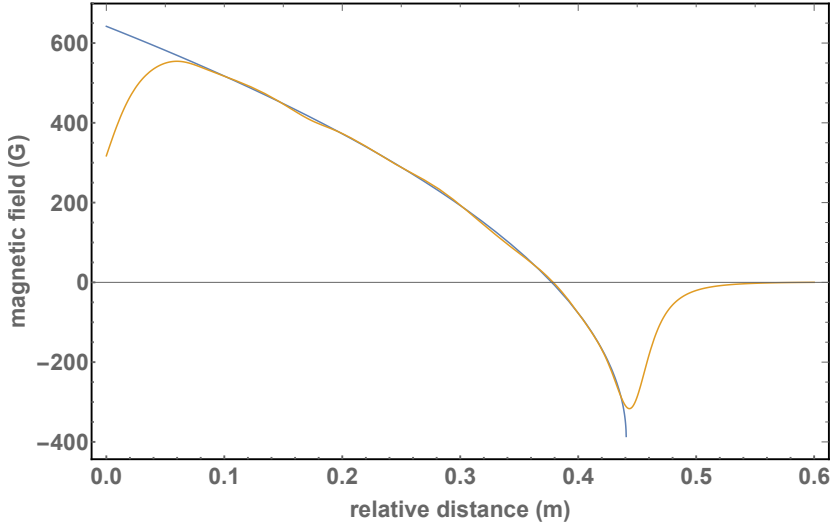


Figure A-2: Simulated magnetic field for the Bitter-type Zeeman slower. Small deviations of around 10 G are still included. To remove them, fine-tuning of each radii has to be done.

The corresponding inner radii a_1 and outer radii a_2 of each copper layer are shown in figure A-3. The tube diameter was set to 28 mm.

Water-cooling the last part turned out to be a large issue. To reach the high magnetic field, either very high currents or small radii were needed. For the simulations a current of -200 A was assumed. Also

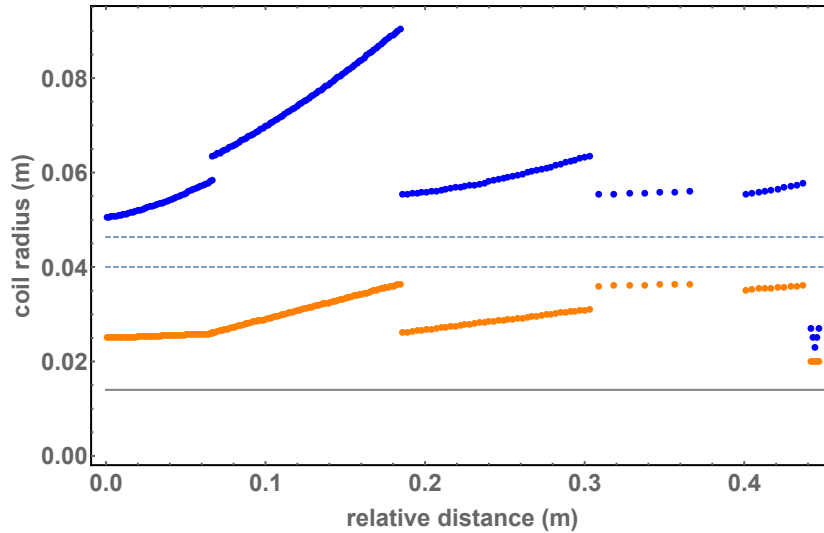


Figure A-3: Simulated inside (orange) and outer (blue) radii for the Bitter-type Zeeman slower. The dashed lines mark the position of the water-cooling. The last part generating the negative magnetic field is not contained in the water-cooling circle. The solid line marks the tube outer diameter.

preventing leaking over the length of the Zeeman slower (45 cm) could be an issue. Pressure has to be applied uniformly on all layers. Additional issues were the large space required and the heavy weight due to the large outer diameter. Therefore the idea of a Bitter-type coil Zeeman slower was dismissed. Instead a conventional design approach was chosen.

A possible solution for the water-cooling problem could be to divide the Zeeman slower in two spatially separated parts. The water-cooling holes can then be positioned at different radii and different minimal and maximal radii for each part can be selected. Separating the Zeeman slower in several parts could also decrease the change of leaks. For smaller parts less layers have to be pressed together, which would result in a more tight compression.

Appendix B

Magnetic field measurements

In this section a short overview over the measurement of the magnetic field during the winding process is given. The magnetic fields was measured with a Honeywell SS496 A1 sensor after each finished winding phase. With the difference between the measured voltage value for zero magnetic field U_0 and a position dependent voltage value U_z , one can calculate the magnetic field by [47]

$$B_z = \frac{U_0 - U_z}{0.002425}.$$

The measured magnetic field was then compared to the simulated magnetic field (following equation 5.9) to check for possible short circuits between the individual layers. In addition, if small deviations would occur, one could correct the winding plan to compensate. That way corrections to the magnetic field can be done during the winding process. Measurements were done with a Hall sensor, taking data every centimetre. To prevent damage to the glue, lower currents were used: $I_1 = 10$ A, $I_2 = 3.333$ A and $I_3 = -6$ A.

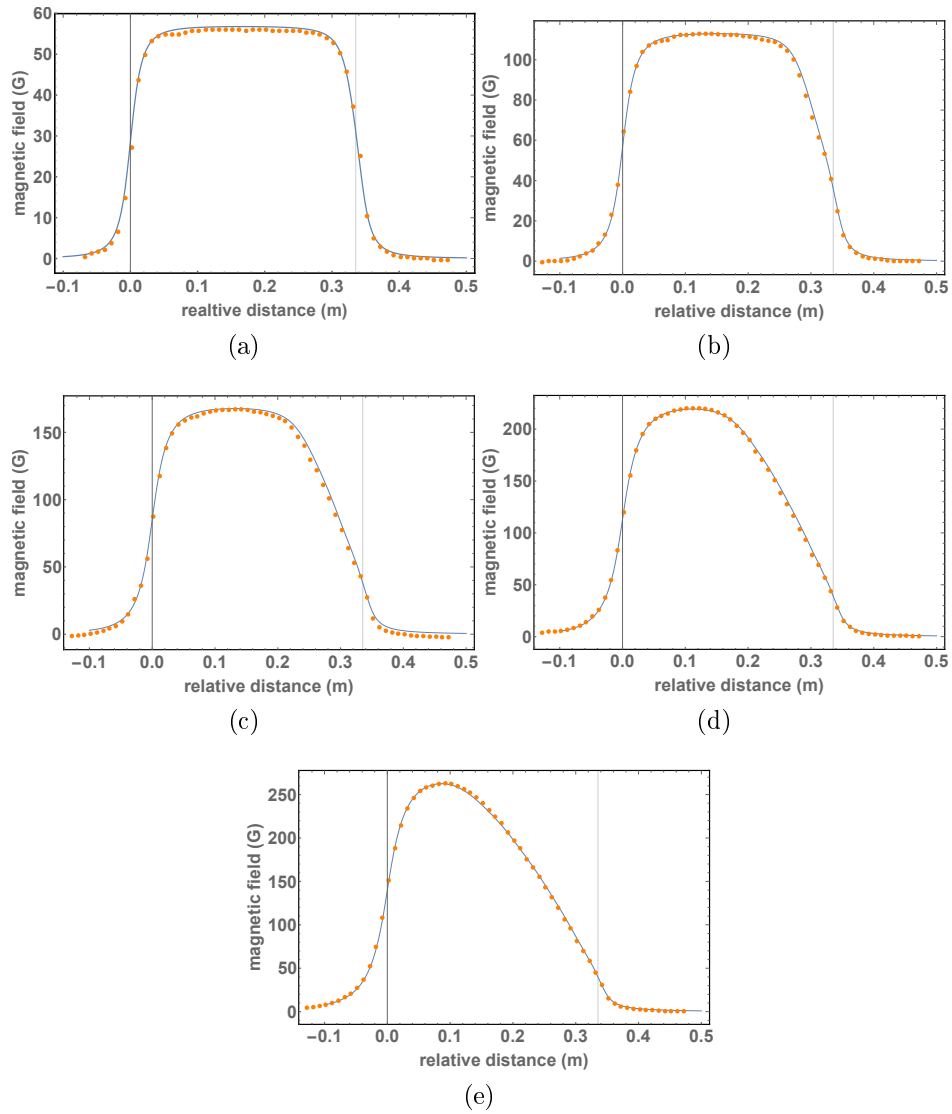


Figure B-1: Magnetic field measurements including the square wire after (a) 2 layers, (b) 4 layers, (c) 6 layers, (d) 8 layers and (e) 10 layers.

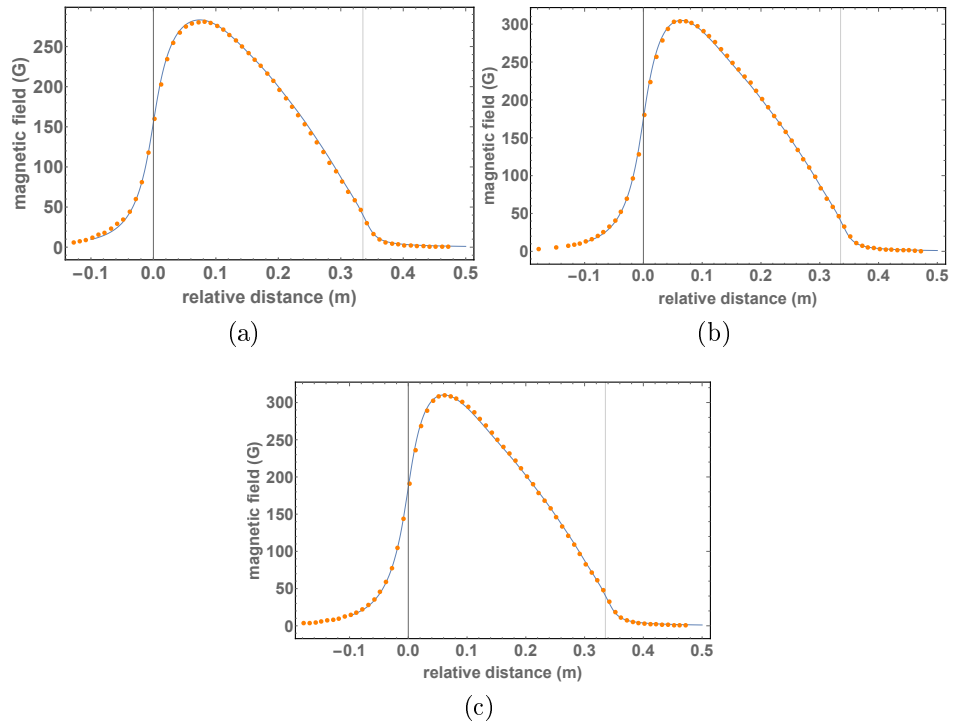


Figure B-2: Magnetic field measurements including the top part after (a) 2 layers, (b) 5 layers and (c) 10 layers.

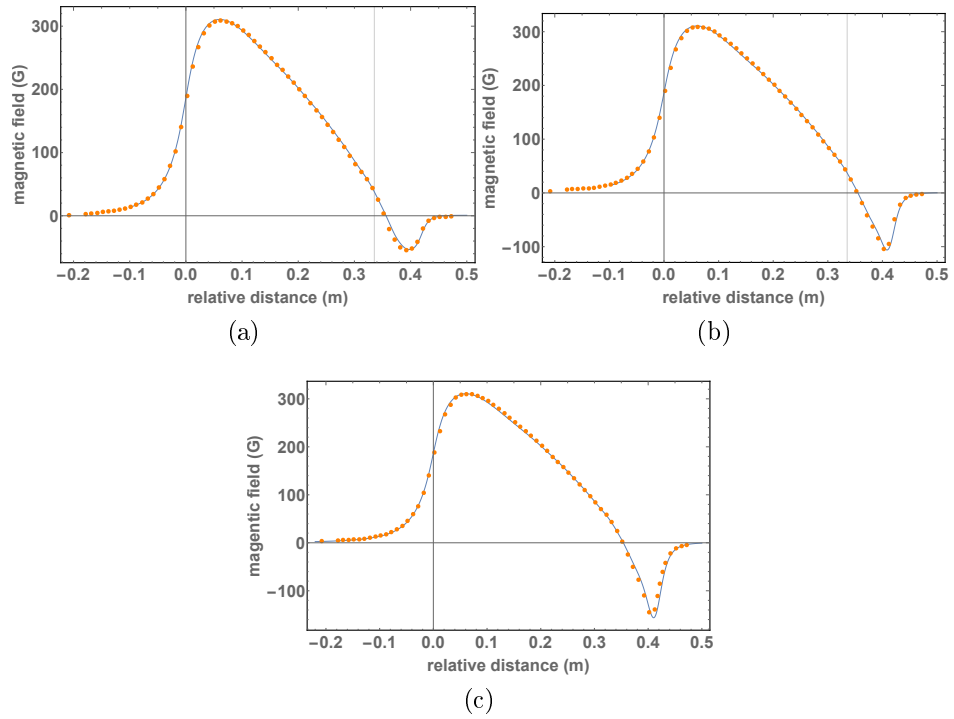


Figure B-3: Magnetic field measurements including the negative current part after (a) 2 layers, (b) 6 layers and (c) 14 layers.

Bibliography

- [1] M. H. Anderson, J. R. Ensher, M. R. Matthews, C. E. Wieman, and E. A. Cornell. *Observation of Bose-Einstein condensation in a dilute atomic vapor*. *Science*, 269 (0) (ii):198, 1995.
- [2] K.B Mavis, M.-O. Mewes, M.R. Andrews, N.J. van Duten, D.S. Durfee, D.M. Kurn, and W. Ketterle. *Bose-Einstein Condensation in a Gas of Sodium Atoms*. *Physical Review Letters*, 75 (November), 1995.
- [3] Albert Einstein. *Quantentheorie des einatomigen idealen Gases*, 1924.
- [4] B. DeMarco. *Onset of Fermi Degeneracy in a Trapped Atomic Gas*. *Science*, 285 (5434):1703–1706, 2002.
- [5] Axel Griesmaier and Sven Hensler. *Bose-Einstein condensation of chromium*. 2005.
- [6] M. A. Baranov, M. Dalmonte, G. Pupillo, and P. Zoller. *Condensed Matter Theory of Dipolar Quantum Gases*. *Chemical Reviews*, 112 (9):5012–5061, 2012.
- [7] T Lahaye, C Menotti, L Santos, M Lewenstein, and T Pfau. *The physics of dipolar bosonic quantum gases*. *Reports on Progress in Physics*, 72 (126401), 2009.
- [8] J. Stuhler. *Observation of dipole-dipole interaction in a degenerate quantum gas*. 2005.
- [9] K. Aikawa, A. Frisch, M. Mark, S. Baier, A. Rietzler, R. Grimm, and F. Ferlaino. *Bose-Einstein condensation of erbium*. *Physical Review Letters*, 108 (21):1–5, 2012.
- [10] K. Aikawa, A. Frisch, M. Mark, S. Baier, R. Grimm, and F. Ferlaino. *Reaching Fermi degeneracy via universal dipolar scattering*. *Physical Review Letters*, 112 (1):1–5, 2014.

- [11] Mingwu Lu, Nathaniel Q. Burdick, and Benjamin L. Lev. *Quantum degenerate dipolar Fermi gas*. Physical Review Letters, 108 (21):1–5, 2012.
- [12] Mingwu Lu, Nathaniel Q. Burdick, Seo Ho Youn, and Benjamin L. Lev. *Strongly dipolar Bose-Einstein condensate of dysprosium*. Physical Review Letters, 107 (19):1–5, 2011.
- [13] Matthias Schmitt, Matthias Wenzel, Fabian Böttcher, Igor Ferrier-Barbut, and Tilman Pfau. *Self-bound droplets of a dilute magnetic quantum liquid*. Nature, 539 (7628):259–262, 2016.
- [14] Matthias Wenzel, Fabian Böttcher, Jan Niklas Schmidt, Michael Eisenmann, Tim Langen, Tilman Pfau, and Igor Ferrier-Barbut. *Anisotropic Superfluid Behavior of a Dipolar Bose-Einstein Condensate*. Physical Review Letters, 121 (3):30401, 2018.
- [15] L Tanzi, E Lucioni, F Fam, J Catani, and A Fioretti. *Observation of a dipolar quantum gas with metastable supersolid properties*. pages 1–12, 2019.
- [16] B Fabian, Jan-niklas Schmidt, Matthias Wenzel, Mingyang Guo, Tim Langen, and Tilman Pfau. *Transient supersolid properties in an array of dipolar quantum droplets*. pages 1–11, 2019.
- [17] L. Chomaz, D. Petter, P. Ilzhöfer, G. Natale, A. Trautmann, C. Politi, G. Durastante, R. M. W. van Bijnen, A. Patscheider, M. Sohmen, M. J. Mark, and F. Ferlaino. *Long-lived and transient supersolid behaviors in dipolar quantum gases*. Physical Review X, 9 (2):21012, 2019.
- [18] Waseem S. Bakr, Jonathon I. Gillen, Amy Peng, Simon Fölling, and Markus Greiner. *A quantum gas microscope for detecting single atoms in a Hubbard-regime optical lattice*. Nature, 462 (7269):74–77, 2009.
- [19] Yamamoto Ryuta, Kobayashi Jun, Kuno Takuma, Kato Kohei, and Takahashi Yoshiro. *An ytterbium quantum gas microscope with narrow-line laser cooling*. New Journal of Physics, 18 (2):23016, 2016.
- [20] D. Studer, L. Maske, P. Windpassinger, and K. Wendt. *Laser spectroscopy of the 1001-nm ground-state transition in dysprosium*. Physical Review A, 98 (4):1–5, 2018.

- [21] M. Rust, M. Bates, and Xiaowei Zhuang. *Stochastic optical reconstruction microscopy (STORM) provides sub-diffraction-limit image resolution (text)*. *Natur Methods*, 3 (10):793–795, 2006.
- [22] Bo Huang, Wenqin Wang, Mark Bates, and Xiaowei Zhuang. *3D super-res imaging by STORM*. *Science*, 319 (5864):810–813, 2008.
- [23] Jonas Fölling, Mariano Bossi, Hannes Bock, Rebecca Medda, Christian A. Wurm, Birka Hein, Stefan Jakobs, Christian Eggeling, and Stefan W. Hell. *Fluorescence nanoscopy by ground-state depletion and single-molecule return*. *Nature Methods*, 5 (11):943–945, 2008.
- [24] J. Dalibard and C. Cohen-Tannoudji. *Laser cooling below the Doppler limit by polarization gradients: simple theoretical models*. *Journal of the Optical Society of America B*, 6 (11):2023, 1989.
- [25] Christopher J. Foot. *Atomic Physics*. Oxford University Press, 2005.
- [26] E. L. Raab, M. Prentiss, Alex Cable, Steven Chu, and D. E. Pritchard. *Trapping of Neutral Sodium Atoms with Radiation Pressure*. *Physical Review Letters*, 59 (23):2631–2634, dec 1987.
- [27] P. Ilzhöfer, G. Durastante, A. Patscheider, A. Trautmann, M. J. Mark, and F. Ferlaino. *Two-species five-beam magneto-optical trap for erbium and dysprosium*. *Physical Review A*, 97 (2):7–12, 2018.
- [28] J.R. De Laeter, J.K. Böhlke, P. De Bièvre, H. Hidaka, H.S. Peiser, K.J.R. Rosman, and P.D.P. Taylor. *Atomic weights of the elements: Review 2000*. *Pure and Applied Chemistry*, 75 (6):683–800, 2003.
- [29] Irina Segal, Ludwik Halicz, and Itzhak T Platzner. *ratio measurements of dysprosium by multiple collection inductively coupled plasma mass spectrometry*. *International Journal of Mass Spectrometry*, 216 (2):177–184, 2002.
- [30] T. Maier, H. Kadau, M. Schmitt, A. Griesmaier, and T. Pfau. *Narrow-line magneto-optical trap for dysprosium atoms*. 39(11):3138–3141, 2014.
- [31] Florian Huber. *Site-Resolved Imaging with the Fermi Gas Microscope*. PhD thesis, 2014.

- [32] Johannes Schindler. *Characterization of an Erbium Atomic Beam*. Master's thesis, 2011.
- [33] John V. Prodan, William D. Phillips, and Harold Metcalf. *Laser production of a very slow monoenergetic atomic beam*. Physical Review Letters, 49 (16):1149–1153, 1982.
- [34] Davide Dreon. *Designing and building an ultracold Dysprosium experiment : a new framework for light-spin interaction*. PhD thesis, 2017.
- [35] Thomas Maier. *Interactions in a Quantum Gas of Dysprosium Atoms*. PhD thesis, 2015.
- [36] Sebastian J Krinner. *Towards Quantum Degenerate Gases of Ytterbium Atoms*. (November), 2010.
- [37] Nicolas Zuber. *Design and setup of an ultracold dual-species Rydberg experiment*. Master's thesis, 2016.
- [38] Sven Kroboth. *Laserkühlung von Ytterbiumatomen*. Diploma thesis, 2002.
- [39] Albert Frisch. *Dipolar Quantum Gases of Erbium by*. PhD thesis, 2014.
- [40] D. E. Gray. *American Institute of Physics Handbook*. American Institute of Physics, 1972.
- [41] John H. Moore, Christopher C. Davis, and Michael A. Coplan. *Building Scientific Apparatus*. Cambridge University Press, 4th edition, 2016.
- [42] Rebecca Grinham and Dr Andrew Chew. *A Review of Outgassing and Methods for its Reduction*. Applied Science and Convergence Technology, 26 (5):95–109, 2017.
- [43] R. Nuvolone. *Technology of low-pressure systems establishment of optimum conditions to obtain low degassing rates on 316 L stainless steel by heat treatments*. Journal of Vacuum Science and Technology, 14 (5):1210–1212, 2002.
- [44] F. Bitter. *The design of powerful electromagnets part III. The use of iron*. Review of Scientific Instruments, 8 (9):318–319, 1937.

- [45] F. Bitter. *The design of powerful electromagnets part II. The magnetizing coil.* Review of Scientific Instruments, 7 (12):482–488, 1936.
- [46] Dylan O. Sabulsky, Colin V. Parker, Nathan D. Gemelke, and Cheng Chin. *Efficient continuous-duty Bitter-type electromagnets for cold atom experiments.* Review of Scientific Instruments, 84 (10):1–5, 2013.
- [47] Honeywell. *High Performance Miniature Ratiometric Linear Hall Effect Sensor*, 2019.